Geophysical Journal International

Geophys. J. Int. (2019) **218,** 1276–1297
Advance Access publication 2019 May 16
GJI Seismology

doi: 10.1093/gji/ggz223

A generalized theory for full microtremor horizontal-to-vertical [H/V(z, f)] spectral ratio interpretation in offshore and onshore environments

Agostiny Marrios Lontsi,[1] Antonio García-Jerez,[2,3] Juan Camilo Molina-Villegas,[4,5] Francisco José Sánchez-Sesma,[6] Christian Molkenthin,[7] Matthias Ohrnberger,[8] Frank Krüger,[8] Rongjiang Wang[9] and Donat Fäh[1]

[1]*Swiss Seismological Service, ETH Zürich, 8092 Zurich, Switzerland. E-mail: agostiny.lontsi@sed.ethz.ch*
[2]*Departamento de Química y Física, Universidad de Almeria, 04120 Almeria, Spain*
[3]*Instituto Andaluz de Geofísica, Universidad de Granada, 18071 Granada, Spain*
[4]*Facultad de Ingenierías, Universidad de Medellín, Carrera 87 No 30-65, Medellín, Colombia*
[5]*Departamento de ingeniería civil, Facultad de Minas, Universidad Nacional de Colombia - Sede Medellín, Carrera 80 No 65-223, Medellín, Colombia*
[6]*Instituto de Ingeniería, Universidad Nacional Autónoma de México, Circuito Escolar s/n, Cd Universitaria, Coyoacán 04510, CDMX, Mexico*
[7]*Institute of Mathematics, University of Potsdam, 14476 Potsdam, Germany*
[8]*Institute of earth and environmental Science, University of Potsdam, 14476 Potsdam, Germany*
[9]*GFZ German Research Centre for Geosciences, 14473 Potsdam, Germany*

Accepted 2019 May 14. Received 2019 May 8; in original form 2019 January 19

SUMMARY

Advances in the field of seismic interferometry have provided a basic theoretical interpretation to the full spectrum of the microtremor horizontal-to-vertical spectral ratio [H/V(f)]. The interpretation has been applied to ambient seismic noise data recorded both at the surface and at depth. The new algorithm, based on the diffuse wavefield assumption, has been used in inversion schemes to estimate seismic wave velocity profiles that are useful input information for engineering and exploration seismology both for earthquake hazard estimation and to characterize surficial sediments. However, until now, the developed algorithms are only suitable for on land environments with no offshore consideration. Here, the microtremor H/V(z, f) modelling is extended for applications to marine sedimentary environments for a 1-D layered medium. The layer propagator matrix formulation is used for the computation of the required Green's functions. Therefore, in the presence of a water layer on top, the propagator matrix for the uppermost layer is defined to account for the properties of the water column. As an application example we analyse eight simple canonical layered earth models. Frequencies ranging from 0.2 to 50 Hz are considered as they cover a broad wavelength interval and aid in practice to investigate subsurface structures in the depth range from a few meters to a few hundreds of meters. Results show a marginal variation of 8 per cent at most for the fundamental frequency when a water layer is present. The water layer leads to variations in H/V peak amplitude of up to 50 per cent atop the solid layers.

Key words: Numerical modelling; Earthquake hazards; Seismic interferometry; Site effects; Theoretical seismology; Wave propagation.

1 INTRODUCTION

Over the past decades, using the single-station microtremor horizontal-to-vertical (H/V) spectral ratio as a method for shallow subsurface characterization has attracted a number of site investigation studies both on land (e.g. Bard 1998; Fäh *et al.* 2003; Scherbaum *et al.* 2003; Lontsi *et al.* 2015, 2016; García-Jerez *et al.* 2016; Piña-Flores *et al.* 2017; Spica *et al.* 2018; García-Jerez *et al.* 2019) and in marine environment (e.g. Huerta-Lopez *et al.* 2003; Muyzert 2007; Overduin *et al.* 2015). The interest in the method is mainly due to its practicability, its cost efficiency, and the minimum investment effort during microtremor (ambient noise or passive seismic) survey campaigns. The generic engineering parameter directly estimated from the spectrum of the microtremor H/V spectral ratio is the site fundamental frequency (e.g. Nakamura 1989; Lachet & Bard 1994). The fundamental frequency of a site generally corresponds to the frequency for which the microtremor H/V spectral ratio reaches its maximum amplitude.

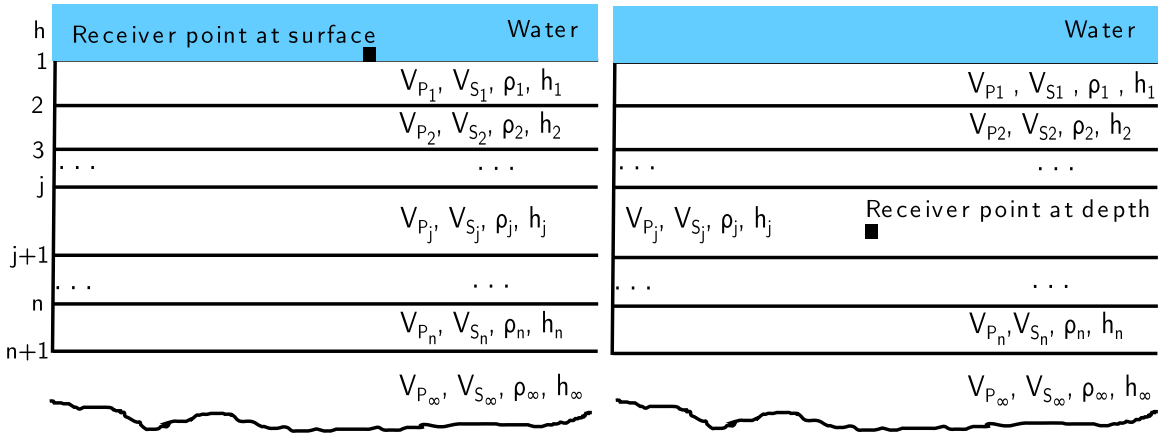

Figure 1. Schematic representation of a 1-D layered medium. The representation without the water layer on top corresponds to the onshore case and the representation with water layer corresponds to the offshore case. For the representation on the left, the receiver location is at the earth's surface when no water layer is present (onshore) and at the water (lake, sea, ocean) bottom when the water layer is present (offshore). For the representation on the right, the receiver location is at depth. Except for the water layer in the offshore case where the shear wave velocity is zero, any other layer j either onshore or offshore is characterized by the seismic parameters V_{P_j}, V_{S_j}, ρ_j, h_j, Q_{P_j} and Q_{S_j}.

Although the peak frequency is relatively well understood, this is not straightforward for secondary peaks as they could represent higher modes or materialize the presence of more than one strong contrast in the subsurface lithology. It is therefore important in the analysis to use a physical formulation for the H/V spectral ratio that not only accounts for the full spectrum (including first and subsequent secondary peaks) but also includes all wave constituent parts. Based upon the advances in seismic noise interferometry (e.g. Lobkis & Weaver 2001; Shapiro & Campillo 2004; Curtis *et al.* 2006; Wapenaar & Fokkema 2006; Sens-Schönfelder & Wegler 2006; Gouédard *et al.* 2008), Sánchez-Sesma *et al.* (2011) proposed a physical model for the interpretation of the full spectrum of the microtremor H/V spectral ratio. This has been extended to include receivers at depths (Lontsi *et al.* 2015). This additional information from receivers at depth is an added value during the velocity imaging process (Lontsi *et al.* 2015; Lontsi 2016; Spica *et al.* 2018). As the interpretation effort focuses on the H/V spectral ratio acquisition on land, no significant effort has been made for the marine acquisition counterpart. An early study for a station on the seafloor was performed by Huerta-Lopez *et al.* (2003), assuming that the wavefield is due to the propagation of an incident plane *SH* body wave. With the evolving technology in borehole acquisition seismic instruments and data transmission (e.g. Stephen *et al.* 1994), there is a growing need for efficient subsea exploration and geohazard estimation as reported by Djikpesse *et al.* (2013).

Here we further extend the diffuse field model (Sánchez-Sesma *et al.* 2011; Lontsi *et al.* 2015) to allow for the interpretation of the H/V(z, f) both in marine sedimentary environment and on land even though applicability to marine environments is emphasized.

The Thomson–Haskell propagator matrix (Thomson 1950; Haskell 1953) is used to relate the displacement and stress for *SH* and *P–SV* waves at two points within an elastic 1-D layered medium. The use of the propagator matrix formulation allows us to easily include a propagator for a layer on top that accounts for the properties of the water layer and to subsequently compute the Green's function for points at different depths. The classical Thomson–Haskell method is unstable when waves become evanescent. To remedy this issue, many attempts have been made (e.g. Knopoff 1964; Dunkin 1965; Abo-Zena 1979; Kennett & Kerry 1979; Harvey 1981; Wang 1999). Here, we use the orthonormalization approach by Wang (1999) which preserves the original Thomson–Haskell matrix algorithm and avoid the loss of precision by inserting an additional procedure that makes *in situ* base vectors orthonormal.

A synthetic analysis is performed on eight simple canonical earth models. The models differ by the presence of soft sediment structures with different overall thickness (two in total) and the presence of a water column with varying depth at the top. The first sediment structure is a very simple one layer over a half-space earth model and the second is a realistic structural model obtained from site characterization at Baar, a municipality in the Canton of Zug, Switzerland. The H/V spectral ratio is estimated for frequencies ranging from 0.2 to 50 Hz. The effects of the water column on the H/V spectrum at selected depths are interpreted.

2 MICROTREMOR H/V SPECTRAL RATIO: A PHYSICAL INTERPRETATION

Here, the main steps linking the microtremor H/V(z, f) spectral ratio to the elastodynamic Green's functions are presented. The basic expressions for *SH* and *P–SV* wave contributions to the Green's functions and some considerations for numerical integration are summarized.

2.1 H/V(z, f) interpretation: onshore case

Starting from three-component ambient vibration data, the microtremor H/V spectral ratio at a given point at the earth's surface or at depth (onshore: Fig. 1 without water layer) for a known frequency f is estimated using eq. (1).

$$H/V(z,\,f) = \sqrt{\frac{E_1(z,\,f) + E_2(z,\,f)}{E_3(z,\,f)}}, \tag{1}$$

where $E_m(z,f) = \rho\omega^2 \langle u_m(z,f) u_m{}^*(z,f)\rangle$ is physically regarded as the directional energy density, ρ is the mass density, ω is the angular frequency and u_m ($m = 1, 2, 3$) is the recorded displacement wavefield in the orthogonal direction m. The indexes $m = 1, 2$ correspond to the horizontal components while $m = 3$ corresponds to the index for the vertical component. The summation convention for repeated indexes is not applied here. The symbol $*$ stands for complex conjugate. Using interferometric principles under the diffuse field assumption, it can be shown that the average of the autocorrelation of the displacement field is proportional to the imaginary part of the Green's function assuming the source and the receivers are at the same point (Sánchez-Sesma *et al.* 2008; Snieder *et al.* 2009, see a summary in Appendix A). Eq. (1) in terms of the Green's function is expressed as

$$\mathrm{H/V}(z,\,f) = \sqrt{\frac{\mathrm{Im}[G_{11}(z,\,z,\,f)] + \mathrm{Im}[G_{22}(z,\,z,\,f)]}{\mathrm{Im}[G_{33}(z,\,z,\,f)]}} = \sqrt{\frac{2\mathrm{Im}[G_{11}(z,\,z,\,f)]}{\mathrm{Im}[G_{33}(z,\,z,\,f)]}}\quad . \tag{2}$$

We are therefore left with the computation of the Green's functions $G_{11} = G_{22}$ and G_{33}. The elastodynamic Green's function in a 1-D elastic layered medium (onshore: Fig. 1 without water layer) is the set of responses for unit harmonic loads in the three directions. Using cylindrical coordinates the contribution of the radial–vertical (*P–SV*) and transverse (*SH*) motions are decoupled. Therefore, it suffices to solve each case separately using the integration on the horizontal wavenumber (Bouchon & Aki 1977).

2.2 *SH* and *P–SV* contribution to the Green's function

Assuming the subsurface structure can be approximated by a stack of homogeneous layers over a half-space as depicted in Fig. 1 where, for example, the *j*th layer is characterized in the onshore case by the compressional wave velocity V_{P_j}, the shear wave velocity V_{S_j}, the density ρ_j, the layer thickness h_j, and the attenuation parameters Q_{P_j} and Q_{S_j} for the *P* and S waves, respectively, $\mathrm{Im}[G_{11}]$, $\mathrm{Im}[G_{22}]$ and $\mathrm{Im}[G_{33}]$ are given by

$$\mathrm{Im}[G_{11}] = \frac{1}{4\pi}\int_0^\infty \mathrm{Im}\,[g_{11\mathrm{SH}}]\,k\mathrm{d}k + \frac{1}{4\pi}\int_0^\infty \mathrm{Im}\,[g_{11\mathrm{PSV}}]\,k\mathrm{d}k \tag{3}$$

$$\mathrm{Im}[G_{33}] = \frac{1}{2\pi}\int_0^\infty \mathrm{Im}\,[g_{33\mathrm{PSV}}]\,k\mathrm{d}k\cdot \tag{4}$$

Because of symmetry, $\mathrm{Im}[G_{11}] = \mathrm{Im}[G_{22}]$. Here k is the radial wavenumber. The kernels $g_{11\mathrm{SH}}$, $g_{11\mathrm{PSV}}$ and $g_{33\mathrm{PSV}}$ correspond to the *SH* and *P–SV* wave contributions. The explicit dependence of $g_{11\mathrm{SH}}$, $g_{11\mathrm{PSV}}$, and $g_{33\mathrm{PSV}}$ on the Thomson–Haskell propagator matrix (2×2 for *SH* waves and 4×4 for *P–SV* waves) for the layered elastic earth model presented in Fig. 1 is given in Appendices B and C.

2.3 H/V(z, f) interpretation: offshore case

In the particular case where the top layer is a perfect homogeneous water layer, the shear wave velocity and shear modulus do not exist (are null). Substituting directly the corresponding properties into the formulae of the 4×4 propagator matrix for *P–SV* waves (eqs C9–C11) leads to a singular matrix. In this limiting case, there is an alternative approach to consider *P* waves along the water column. A pseudo 4×4 propagator matrix $\mathbf{P}_{\mathrm{pseudo}}$ is defined (eq. 5) and treated as in the onshore case (Herrmann 2008):

$$\mathbf{P}_{\mathrm{pseudo}} = \begin{pmatrix} 1 & 0 & 0 & 0 \\ 0 & \cosh(\gamma h) & 0 & -\dfrac{\gamma}{\rho\omega}\sinh(\gamma h) \\ 0 & 0 & 1 & 0 \\ 0 & -\dfrac{\rho\omega^2}{\gamma}\sinh(\gamma h) & 0 & \cosh(\gamma h) \end{pmatrix}, \tag{5}$$

where $\gamma = \sqrt{k^2 - \omega^2/V_{\mathrm{P}}^2}$ represents the vertical wavenumber for *P* wave in water and h the thickness of the water column. A full derivation of $\mathbf{P}_{\mathrm{pseudo}}$ is presented in Appendix E.

2.4 Considerations for numerical implementation

For the numerical integration, eqs (3) and (4) are transformed into a summation assuming virtual sources spread along the horizontal plane with generic spacing L (Bouchon & Aki 1977). The parameter L also defines the integration step $\mathrm{d}k = \dfrac{2\pi}{L}$. The vertical wavenumbers γ_j and ν_j for, respectively, *P* and *S* waves in the *j*th layer relate to the horizontal wavenumbers k by

$$\gamma_j = \sqrt{k^2 - \frac{\omega^2}{V_{\mathrm{P}_j}^2}} \tag{6}$$

Table 1. Seismic parameters for a homogeneous half-space. The model is used to estimate the directional energy density profile with normalized depth.

h (m)	V_P (m s^{-1})	V_S (m s^{-1})	ρ (kg m^{-3})	Q_P	Q_S
∞	1732	1000	2000	100	100

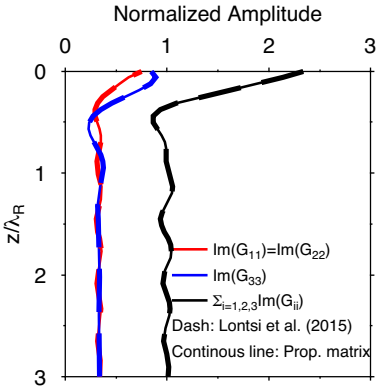

Figure 2. Normalized energy density profiles (Im(G_{11}), Im(G_{22}), Im(G_{33}) and the total directional energy density) for the three orthogonal directions estimated using (1) the algorithm based on the propagator matrix formulation (thin continuous line) and (2) the algorithm based on the global matrix formulation for a layered medium (dashed thick line; Lontsi *et al.* 2015). The depth is normalized with the Rayleigh wavelength. There is a good agreement between the two approaches for Green's functions estimation. Input parameters used in the modelling are defined in Table 1.

$$\nu_j = \sqrt{k^2 - \frac{\omega^2}{V_{S_j}^2}}. \tag{7}$$

Because of pole singularities of the kernel that account for the effects of surface waves, a stable integration on the real axis can be performed if a correction term ω_I is added to the frequency to shift the poles of the kernel from the real axis, so that the effective frequency is

$$\omega = 2\pi f + \omega_I i, \tag{8}$$

where i is the unit imaginary number. ω_I is chosen as the smallest constant that effectively smooth out the kernels. Anelastic attenuation of *P*- and *S*-wave energy is considered by defining complex seismic wave velocities (see e.g. Müller 1985).

Additional considerations are made to avoid the loss-of-precision associated with the Thomson–Haskell propagator matrix when waves become evanescent. A numerical procedure is inserted into the matrix propagation loop to make all determined displacement vectors *in situ* orthonormal (Wang 1999). The orthonormalization procedure, as implemented here, for both surface downward- and infinity upward wave propagation of the determined base vectors is presented in Appendix D.

3 SYNTHETIC ANALYSIS USING CANONICAL AND REALISTIC EARTH MODELS

For testing the presented algorithm, the directional energy density profile for a homogeneous half-space is computed. Table 1 presents the model parameters for this simple earth structure defined as a Poisson solid.

The energy variation with depth as depicted in Fig. 2 shows a good agreement with the known theory regarding the energy partition for a diffuse wavefield (e.g. Weaver 1985; Perton *et al.* 2009). For depths larger than approximately 1.5 times the Rayleigh wavelength, there is almost no surface wave energy contribution and the energy is equal for the three orthogonal directions (Fig. 2).

Further tests are performed by considering a simple one layer over a half-space (1LOH) and a realistic subsurface structure. The realistic earth model has been obtained from site characterization at Baar, Canton Zug, Switzerland (Hobiger *et al.* 2016). The parameters for the simple 1LOH model together with those of the realistic earth structure used in the second test are presented in Table 2. The 1LOH structural model represents a very simple soft-soil characterized by a constant shear wave velocity (V_S) of 200 m s^{-1}, a velocity contrast of 5 in V_S and an overall sediment cover of 25 m. The realistic earth model at Baar has velocity contrast in V_S of about 4 between the sediment layer overlaying the half-space and the half-space. Here, the overall sediment cover is about 100 m. In comparison to V_S values that remain almost constant, water saturated sediment offshore has compressional wave velocity estimates that are much larger than the onshore values.

Figs 3(a) and 4(a), respectively, present the seismic velocity profiles (V_P and V_S) for the two investigated structural models. Considered V_P profiles for the water saturated sediments are represented by the blue solid line. The corresponding H/V(z, f) spectral ratio without a water layer (onshore) and with water layer (offshore) are plotted together for different depths. This representation allows for a visual appraisal of the effect of the water column (Figs 3b–d and 4b–d).

Table 2. Test models consisting of one and three solid layers over a half-space (onshore). Offshore cases, characterized by $V_S = 0\ \mathrm{m\,s^{-1}}$, are built by considering a water layer on top. In the case where the water layer is considered, the V_P velocities for the sediment at the bottom of the water column are modified to account for the saturation with water. Considered values for V_P are shown in parenthesis in the appropriated column. Scenarios for different water environments ranging from shallow to deep are considered. The H/V spectral ratios at three different locations (surface + two additional depths) for these two illustrative cases are presented in Figs 3 and 4.

h (m)	V_P ($\mathrm{m\,s^{-1}}$)	V_S ($\mathrm{m\,s^{-1}}$)	ρ ($\mathrm{kg\,m^{-3}}$)	Q_P	Q_S
One-layer over a half-space					
8[a](200[b],5000[c])	1500	0	1000	99999	99999
25	500 (1700)	200	1900	100	100
∞	2000	1000	2500	200	200
Realistic earth model at Baar, Canton Zug					
8[a](200[b],5000[c])	1500	0	1000	99999	99999
5.3	672.8 (1600)	85.6	2000	100	100
29.2	738.9 (1600)	284.3	2000	100	100
68.4	2135.6	500.0	2000	100	100
∞	3512.2	1841.1	2300	100	100

[a] Thin water layer. [b] Lake environment. [c] Deep ocean environment.

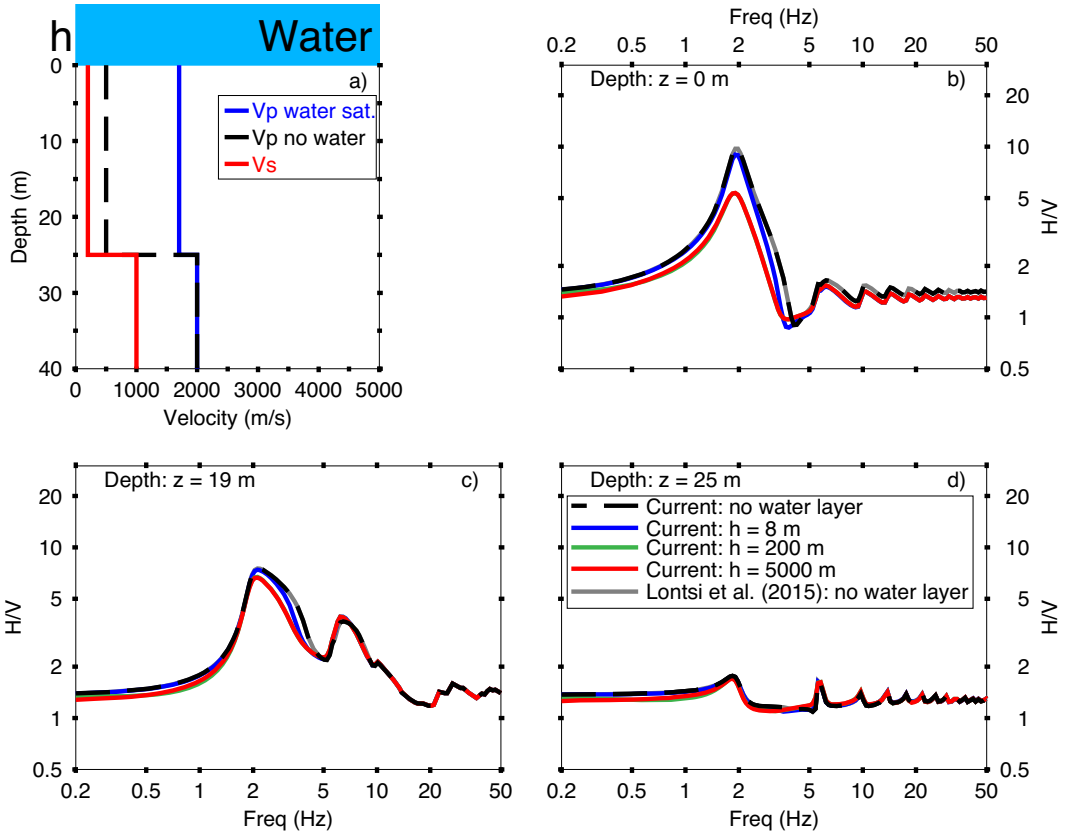

Figure 3. (a) Seismic parameters for a simple soft soil layer over a half-space (defined in Table 2). The *P*-wave velocity in water is set to $1500\ \mathrm{m\,s^{-1}}$. The water-saturated sediments have the velocity set to $1700\ \mathrm{m\,s^{-1}}$ (see solid blue profile). The shear wave velocity (V_S) profile is set unchanged in the presence of the water layer. (b) Comparison between H/V spectral ratios at the solid–liquid interface ($z = 0$ m). (c) Comparison between H/V spectral ratios at 19 m depth and (d) at 25 m depth. The grey curve is obtained using the extended global matrix formulation for receivers at depth when no water layer is present (see Lontsi *et al.* 2015). The computed H/V for a synthetic water layer of 200 and 5000 m shows nearly the same results and are almost overlaid with each other; see green and red curves.

The H/V(z, f) spectral ratio computed with the propagator matrix algorithm for the 1LOH is calibrated with results obtained using the global matrix formulation approach as presented by Lontsi *et al.* (2015) for receivers at depth when no water layer is present (compare solid grey and dashed black lines on Figs 3b–d). The two approaches (propagator matrix and global matrix formulations) provide H/V spectral ratios that agree with each other for all tested receiver locations for the onshore case.

The presented algorithm is further used to assess the variations of the H/V spectral ratios, at the surface and at depth, due to the presence of the water layer. To this end, the structural models presented in Table 2 with three different water-layer thicknesses (8, 200 and 5000 m) are used. The water layer thicknesses are selected to reflect different water environments ranging from shallow lake to deep sea. For the

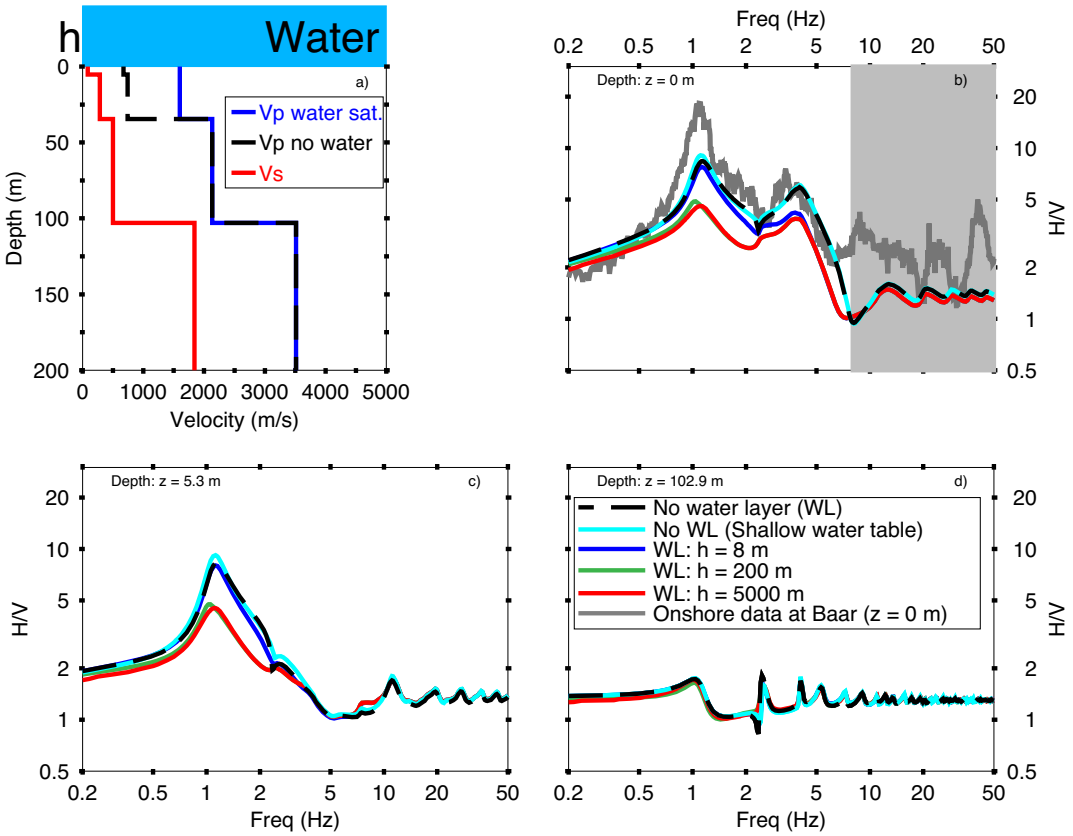

Figure 4. (a) Seismic parameters for a realistic earth model (defined in Table 2). The *P*-wave velocity for water is set to 1500 m s^{-1}. The *P*-wave velocity for water-saturated sediments is represented with the solid blue profile. The shear wave velocity (V_S) profile is set unchanged in the presence of the water layer. In addition, a sedimentary environment with a very shallow water table is considered. The V_P for the sediment in this onshore case was set to 1600 m s^{-1}. (b) Comparison between H/V spectral ratios at the solid-free surface and solid–liquid interface ($z = 0$ m). For the solid-free surface interface (onshore), field data exist and are used for validation of the presented algorithm (solid grey curve). Frequencies above 8 Hz (light grey box) were not used for the profile estimation. (c) Comparison between H/V spectral ratios at 5.3 m within the sediment column and (d) at 102.9 m depth (sediment bedrock interface).

1LOH structural model and for a scenario of shallow water environment with 8 m water column, we observe at frequencies above 2 Hz (peak frequency) an amplitude variation. Further scenarios with moderate (200 m) to deep (5000 m) water layer indicate that the amplitude variations extend to low frequencies and reach up to 50 per cent around the H/V spectral ratio peak amplitude for the receiver at the surface. Only marginal relative variations are observed for the H/V peak frequency when the water layer is present. The amplitude variation as well as the marginal peak frequency variation observed for the 1LOH in different water environments is also valid for the realistic earth model at Baar. For this particular test site, we further consider that the water table is very shallow and investigate the onshore scenario with water saturated sediments' cover. The V_P velocity for the first two layers was set to $V_P = 1600$ m s^{-1} to consider the saturation with water. The resulting H/V spectral ratio computed at different depths indicates that changes in V_P do have influence on the shape of the H/V spectral ratio in the frequency band ranging from about 1 to 3 Hz for receivers at the surface and at depths, although very minor (see Figs 4b–d). At Baar, onshore ambient vibrations data from array recordings are available. The surface waves' analysis allowed to extract the average seismic velocity profiles of the underlying subsurface structure (for more details, see Hobiger *et al.* 2016). The estimated velocity profiles did not account for H/V information beyond 8 Hz shown in the light grey box (Fig. 4b). The H/V spectral ratio from the array central station is used for calibration (grey curve in Fig. 4b).

Within the sediment column, and for all considered water column thicknesses, the variability of the H/V spectral ratio is observed up to a certain cut-off frequency. This cut-off frequency is about 5 Hz at 19 m depth for the 1LOH structural model. For the realistic earth model at Baar and for a receiver at about 5.3 m depth, the cut-off frequency is about 10 Hz. In the last case where the receiver is located at the bedrock interface, marginal H/V amplitude variations are observed (Figs 3d and 4d). For both models, the low-frequency peak corresponds well with the fundamental resonance of *SH* waves in the structure. In the case of the layer above the half-space it is given by the simple relationship $f_0 = \frac{V_S}{4H}$, where H is the thickness of the sediment column and V_S is the shear wave velocity ($Vs = 200$ m s^{-1} and $H = 25$ m, Fig. 3a). For the realistic model at Baar (Fig. 4a), the peak frequency can be estimated by using the simple expression found by Tuan *et al.* (2016) with about 10 per cent deviation. Secondary peaks for the simple 1LOH (Fig. 3a) satisfy the relationship $f_n = \frac{V_S}{4H}(2n + 1)$. For the realistic earth model at Baar (Fig. 4), the second dominant peak at about 4 Hz corresponds to the response of the top layer characterized by a shear wave velocity

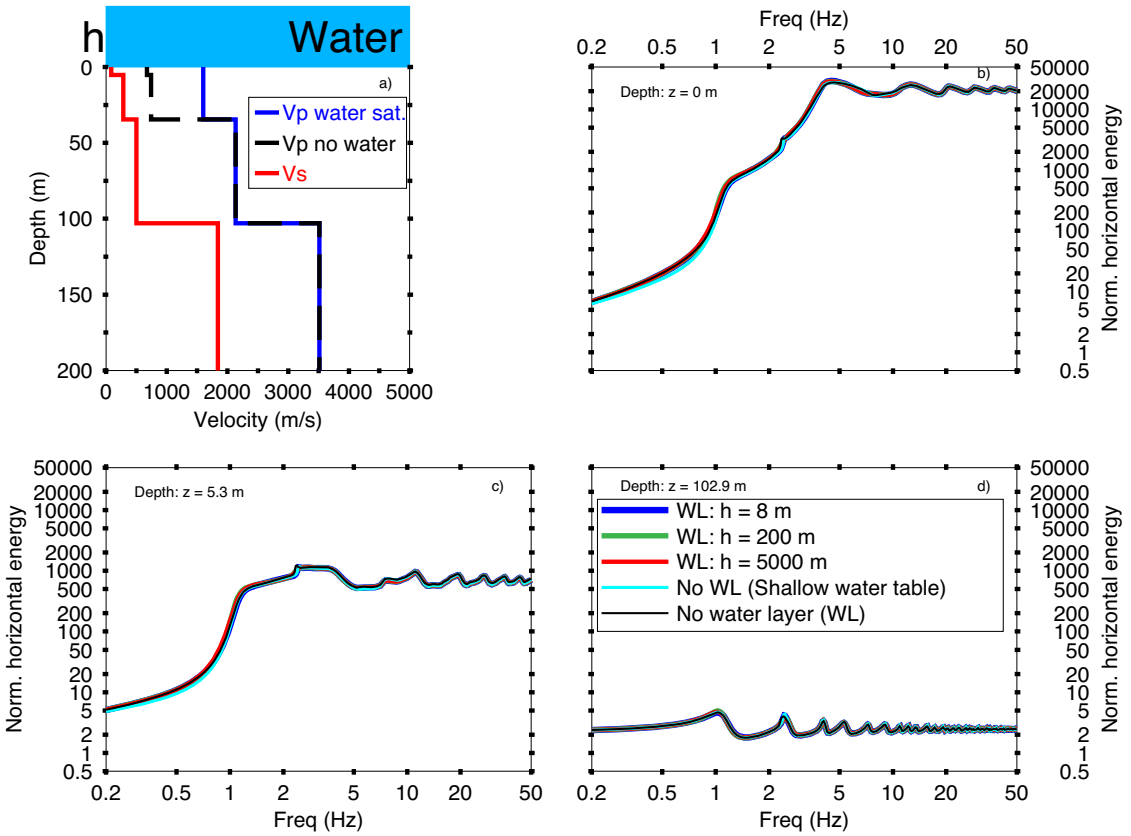

Figure 5. Horizontal directional energy density variation at the seabottom using the structural earth model at Baar. Different water layer thicknesses are considered.

$Vs = 85$ m s^{-1}. The corresponding impedance contrast is about 3.34. A weak impedance contrast of about 1.76 exists between the second and third layers. Additional peaks (grey box, Fig. 4b) would depend on very shallow features not represented by the considered velocity model.

4 UNDERSTANDING THE H/V AMPLITUDE VARIATION

The observed amplitude variation of the H/V in the presence of the water layer is investigated by analysing the modelled directional energy densities (DEDs) both on the horizontal and vertical components. The earth model at Baar is used for the analysis. Figs 5 and 6 show the modelled DEDs for the horizontal and vertical components, respectively. Considered scenarios include an earth model (1) without water layer, (2) with no water layer but very shallow water table, (3) with water layer of 8, 200 and 5000 m. It comes out that the energy on the horizontal component is not sensitive to the presence of the water layer. This is understood as no shear wave is expected to propagate in the considered ideal fluid (no viscosity). On the contrary, we observe significant energy variations on the vertical component that can be associated with multiple energy reverberations in the water layer.

We further assess the dependence of the amplitude variation with a much larger number of water layer thickness scenario. For this purpose, the relative variation of H/V spectral ratio when there is water layer is studied. Fig. 7 depicts this relative variations in per cent for a wide range of water columns. It can be observed that the presence of a shallow water layer mainly has effects on very high frequency. Deep water environment affects the amplitude of the H/V spectral ratio on a very broad frequency range.

5 CONCLUSIONS

A theoretical model based on the diffuse field approximation is proposed for the estimation of the H/V(z, f) spectral ratio on land and in marine environment. The propagator matrix method has been used to compute the Green's function in a 1-D layered medium including a liquid layer atop. For onshore cases, the modelled H/V(z, f) spectral curves are compared with estimations from the global matrix approach and show good agreement for the considered synthetic structural models. In comparison to the global matrix method, the propagator matrix provides an efficient approach for modelling the H/V spectral ratio within marine environments. Modelling results indicate that the H/V spectral ratio is sensitive to the presence of a water layer overlying subseabed sediments. H/V relative amplitude variations are observed in the complete considered frequency range (0.2–50 Hz) for deep water environment and may reach approximately 50 per cent around the peak frequency. The amplitude decrease in the H/V peak can be understood as large P-wave energy on the vertical component result from multiple

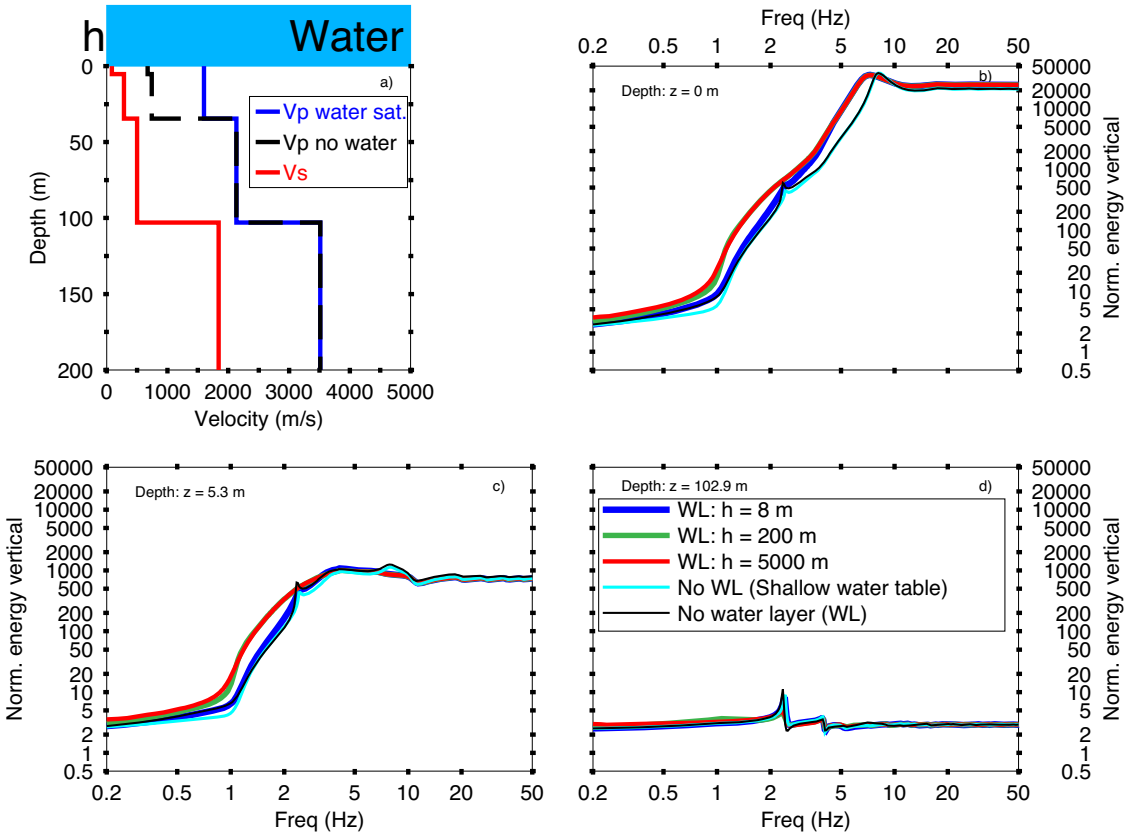

Figure 6. Vertical directional energy density variation at the seabottom using the structural earth model at Baar. Different water layer thicknesses are considered.

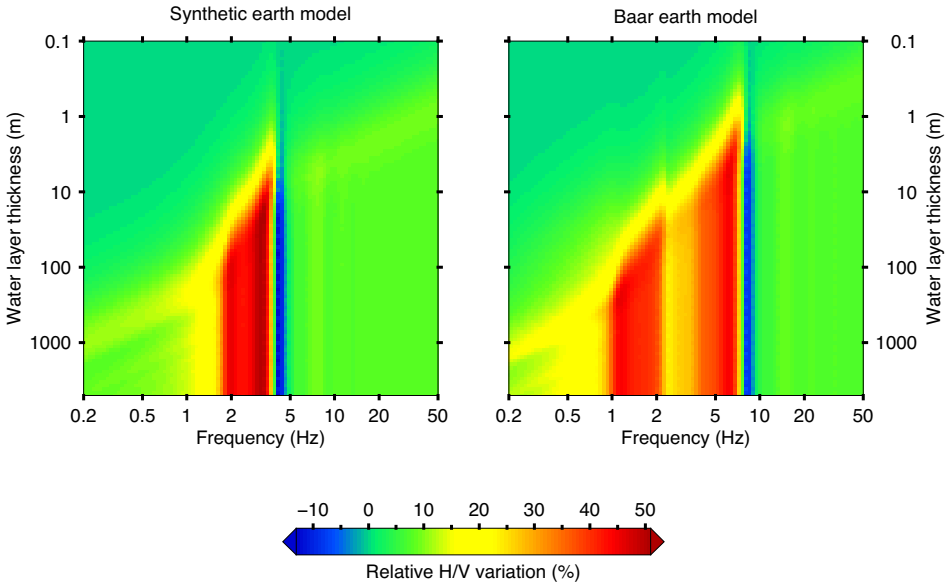

Figure 7. Relative variation of the H/V spectral ratio in the presence of the water layer with respect the H/V spectral ratio when no water layer is present. Water layer thicknesses ranging between 0.1 and 5000 m, sampled on a logarithmic scale are considered. Left: one layer over half-space structure. Right: realistic earth model at Baar.

reverberation in the water column. The H/V data available at Baar (onshore) are used to validate the presented algorithm for a receiver at the surface. For computed cases, changes in the fundamental frequency are marginal. In addition, primary resonances occur at frequencies that satisfy the relationships used in practical applications. Secondary resonances in the 1LOH corresponds to overtones while in the realistic case at Baar, they materialize the response of the subsequent layers within the sediment column.

ACKNOWLEDGEMENTS

Our thanks to F. Luzón for his comments and suggestions and to J. E. Plata and G. Sánchez of the USI-Inst. Eng.-UNAM for locating useful references. This work has been partially supported, through the sinergia program, by the Swiss National Science Foundation (grant 171017), by the Spanish Ministry of Economy and Competitiveness (grant CGL2014-59908), by the European Union with ERDF, by DGAPA-UNAM (Project IN100917) and by the Deutsche Forschungsgemeinschaft (DFG) through grant CRC 1294 'Data Assimilation' (Project B04). Constructive comments from the editors Jörg Renner and Jean Virieux, Hiroshi Kawase and two anonymous reviewers helped to improve the quality of the manuscript.

REFERENCES

Abo-Zena, A., 1979. Dispersion function computations for unlimited frequency values, *Geophys. J. Int.,* **58**(1), 91–105.

Aki, K. & Richards, P.G., 2002. Quantitative Seismology, 2nd edn, *University Science Books*.

Bard, P.-Y., 1998. Microtremor measurements: a tool for site effect estimation? State-of-the-art paper , eds Irikura, K., Kudo, K., Okada, H., Satasini, T. &Balkema, , in *Second International Symposium on the Effects of Surface Geology on Seismic Motion,* Vol. **3,** pp. 1251–1279.

Bouchon, M. & Aki, K., 1977. Discrete wave-number representation of seismic-source wave fields, *Bull. seism. Soc. Am.,* **67**(2), 259–277.

Curtis, A., Gerstoft, P., Sato, H., Snieder, R. & Wapenaar, K., 2006. Seismic interferometry—turning noise into signal, *Leading Edge,* **25**(9), 1082–1092.

Djikpesse, H. *et al.*, 2013. Recent advances and trends in subsea technologies and seafloor properties characterization, *Leading Edge,* **32**(10), 1214–1220.

Domínguez, J. & Abascal, R., 1984. On fundamental solutions for the boundary integral equations method in static and dynamic elasticity, *Engi. Anal.,* **1**(3), 128–134.

Dunkin, J.W., 1965. Computation of modal solutions in layered, elastic media at high frequencies, *Bull. seism. Soc. Am.,* **55**(2), 335–358.

Fäh, D., Kind, F. & Giardini, D., 2003. Inversion of local S-wave velocity structures from average H/V ratios, and their use for the estimation of site-effects, *J. Seismol.,* **7**(4), 449–467.

Gantmacher, F., 1959. *The Theory of Matrices,* Vol. **1,** Chelsea Publishing Company.

García-Jerez, A., Piña-Flores, J., Sánchez-Sesma, F.J., Luzón, F. & Perton, M., 2016. A computer code for forward calculation and inversion of the H/V spectral ratio under the diffuse field assumption, *Comput. Geosci.,* **97,** 67–78.

García-Jerez, A., Seivane, H., Navarro, M., Martínez-Segura, M. & Piña-Flores, J., 2019. Joint analysis of Rayleigh-wave dispersion curves and diffuse-field HVSR for site characterization: the case of El Ejido town (SE Spain), *Soil Dyn. Earthq. Eng.,* **121,** 102–120.

Gilbert, F. & Backus, G.E., 1966. Propagator matrices in elastic wave and vibration problems, *Geophysics,* **31**(2), 326–332.

Gouédard, P. *et al.*, 2008. Cross-correlation of random fields: mathematical approach and applications, *Geophys. Prospect.,* **56**(3), 375–393.

Harvey, D.J., 1981. Seismogram synthesis using normal mode superposition: the locked mode approximation, *Geophys. J. Int.,* **66**(1), 37–69.

Haskell, N.A., 1953. The dispersion of surface waves on multilayered media, *Bull. seism. Soc. Am.,* **43**(1), 17–34.

Herrmann, R.B., 2008. *Seismic Waves in Layered Media,* draft, pp. 1–335.

Hobiger, M., Fäh, D., Michel, C., Burjánek, J., Maranò, S., Pilz, M., Imperatori, W. & Bergamo, P., 2016. Site characterization in the framework of the renewal of the Swiss Strang Motion Network (SSMNet), in *5th IASPEI/IAEE International Symposium: Effects of Surface Geology on Seismic Motion,* Taipei, Taiwan, August 15-17, 2016.

Huerta-Lopez, C., Pulliam, J. & Nakamura, Y., 2003. In situ evaluation of shear-wave velocities in seafloor sediments with a broadband ocean-bottom seismograph, *Bull. seism. Soc. Am.,* **93**(1), 139–151.

Kennett, B. L.N. & Kerry, N.J., 1979. Seismic waves in a stratified half space, *Geophys. J. R. astr. Soc.,* **57**(3), 557–583.

Knopoff, L., 1964. A matrix method for elastic wave problems, *Bull. seism. Soc. Am.,* **54**(1), 431–438.

Lachet, C. & Bard, P.-Y., 1994. Numerical and theoretical investigations on the possibilities and limitations of Nakamura's technique, *J. Phys. Earth,* **42**(5), 377–397.

Lobkis, O.I. & Weaver, R.L., 2001. On the emergence of the Green's function in the correlations of a diffuse field, *J. acoust. Soc. Am.,* **110**(6), 3011–3017.

Lontsi, A.M., 2016, 1D shallow sedimentary subsurface imaging using ambient noise and active seismic data, *Doctoral thesis,* Universität Potsdam.

Lontsi, A.M., Sánchez-Sesma, F.J., Molina-Villegas, J.C., Ohrnberger, M. & Krüger, F., 2015. Full microtremor H/V(z, f) inversion for shallow subsurface characterization, *Geophys. J. Int.,* **202**(1), 298–312.

Lontsi, A.M., Ohrnberger, M., Krüger, F. & Sánchez-Sesma, F.J., 2016. Combining surface wave phase velocity dispersion curves and full microtremor horizontal-to-vertical spectral ratio for subsurface sedimentary site characterization, *Interpretation,* **4**(4), doi:10.1190/INT-2016-0021.1.

Müller, G., 1985. The reflectivity method: a tutorial, *J. Geophys.,* **58,** 153–174.

Muyzert, E., 2007. Seabed property estimation from ambient-noise recordings: Part 2—Scholte-wave spectral-ratio inversion, *Geophysics,* **72**(4), U47–U53.

Nakamura, Y., 1989. A method for dynamic characteristics estimations of subsurface using microtremors on the ground surface, *Q. Rep. RTRI,* **30,** 25–33.

Overduin, P.P., Haberland, C., Ryberg, T., Kneier, F., Jacobi, T., Grigoriev, M.N. & Ohrnberger, M., 2015. Submarine permafrost depth from ambient seismic noise, *Geophys. Res. Lett.,* **42**(18), 7581–7588.

Paul, A., Campillo, M., Margerin, L., Larose, E. & Derode, A., 2005. Empirical synthesis of time-asymmetrical Green functions from the correlation of coda waves, *J. geophys. Res.,* **110**(B8), doi:10.1029/2004JB003521.

Perton, M., Sánchez-Sesma, F.J., Rodríguez-Castellanos, A., Campillo, M. & Weaver, R.L., 2009. Two perspectives on equipartition in diffuse elastic fields in three dimensions, *J. acoust. Soc. Am.,* **126**(3), 1125–1130.

Piña-Flores, J., Perton, M., García-Jerez, A., Carmona, E., Luzón, F., Molina-Villegas, J.C. & Sánchez-Sesma, F.J., 2017. The inversion of spectral ratio H/V in a layered system using the diffuse field assumption (DFA), *Geophys. J. Int.,* **208**(1), 577–588.

Sánchez-Sesma, F.J. & Campillo, M., 2006. Retrieval of the Green's function from cross correlation: the canonical elastic problem, *Bull. seism. Soc. Am.,* **96**(3), 1182–1191.

Sánchez-Sesma, F.J., Pérez-Ruiz, J.A., Luzón, F., Campillo, M. & Rodríguez-Castellanos, A., 2008. Diffuse fields in dynamic elasticity, *Wave Motion,* **45,** 641–654.

Sánchez-Sesma, F.J. *et al.*, 2011. A theory for microtremor H/V spectral ratio: application for a layered medium, *Geophys. J. Int.,* **186**(1), 221–225.

Sánchez-Sesma, F.J., Victoria-Tobon, E., Carbajal-Romero, M., Rodríguez-Sánchez, J.E. & Rodríguez-Castellanos, A., 2018. Energy equipartition in theoretical and recovered seismograms, *J. Appl. Geophys.,* **150,** 153–159.

Scherbaum, F., Hinzen, K.-G. & Ohrnberger, M., 2003. Determination of shallow shear wave velocity profiles in the Cologne, Germany area using ambient vibrations, *Geophys. J. Int.,* **152**(3), 597–612.

Sens-Schönfelder, C. & Wegler, U., 2006. Passive image interferometry and seasonal variations of seismic velocities at Merapi Volcano, Indonesia, *Geophys. Res. Lett.,* **33**(21), doi:10.1029/2006GL027797.

Shapiro, N.M. & Campillo, M., 2004. Emergence of broadband Rayleigh waves from correlations of the ambient seismic noise, *Geophys. Res. Lett.,* **31**(7), doi:10.1029/2004GL019491.

Snieder, R., Wapenaar, K. & Wegler, U., 2007. Unified Green's function retrieval by cross-correlation; connection with energy principles, *Phys. Rev. E,* **75,** 036103 .

Snieder, R., Sánchez-Sesma, F.J. & Wapenaar, K., 2009. Field fluctuations, imaging with backscattered waves, a generalized energy theorem, and the optical theorem, *SIAM J. Imaging Sci.,* **2**(2), 763–776.

Spica, Z.J., Perton, M., Nakata, N., Liu, X. & Beroza, G.C., 2018. Site characterization at Groningen gas field area through joint surface-borehole H/V analysis, *Geophys. J. Int.,* **212**(1), 412–421.

Stephen, R.A. *et al.*, 1994. The Seafloor Borehole Array Seismic System (SEABASS) and VLF ambient noise, *Mar. Geophys. Res.,* **16**(4), 243–286.

Thomson, W.T., 1950. Transmission of elastic waves through a stratified solid medium, *J. Appl. Phys.,* **21**(2), 89–93.

Tuan, T.T., Vinh, P.C., Ohrnberger, M., Malischewsky, P. & Aoudia, A., 2016. An improved formula of fundamental resonance frequency of a layered half-space model used in H/V ratio technique, *Pure appl. Geophys.,* **173**(8), 2803–2812.

van Manen, D.-J., Curtis, A. & Robertsson, J.O., 2006. Interferometric modeling of wave propagation in inhomogeneous elastic media using time reversal and reciprocity, *Geophysics,* **71**(4), SI47–SI60.

Wang, R., 1999. A simple orthonormalization method for stable and efficient computation of Green's functions, *Bull. seism. Soc. Am.,* **89**(3), 733–741.

Wapenaar, K. & Fokkema, J., 2006. Green's function representations for seismic interferometry, *Geophysics,* **71**(4), SI33–SI46.

Weaver, R.L., 1985. Diffuse elastic waves at a free surface, *J. acoust. Soc. Am.,* **78,** 131–136.

APPENDIX A: AMBIENT NOISE–GREEN'S FUNCTION–REPRESENTATION THEOREM–CROSS-CORRELATION–DIRECTIONAL ENERGY DENSITY–EQUIPARTITION

Seismic sources at the origin of the ambient noise wavefield are ubiquitous and may be at surface or/and at depth. Generated seismic waves are back-scattered in the subsurface. The recorded noise wavefield at a seismic station after a lapse time large enough compared to the mean traveltime of ballistic waves (e.g. direct waves, first reflected waves) contains information regarding the underlying subsurface structure.

Let us assume that there is an asymptotic regime with a stable supply of energy that constitutes the background illumination. This condition, for what it shares with the radiative transport, is called diffuse field. In an unbounded elastic medium a harmonic diffuse field is considered random, isotropic and equipartitioned. The stabilization of the S to P energy ratio is reached asymptotically for long lapse times (Paul *et al.* 2005). Within such a field the DED, E_m, for a given orthogonal direction m is given in terms of the averaged autocorrelation of the displacement wavefield and it is proportional to the imaginary part of the Green's function of the system for the source and the receiver at the same location. This is expressed in eq. (A1):

$$E_m(\mathbf{x}, f) = \rho\omega^2 \langle u_m(\mathbf{x}, f) u_m^*(\mathbf{x}, f)\rangle \propto \mathrm{Im}[G_{mm}(\mathbf{x}, \mathbf{x}, f)]. \tag{A1}$$

Here $\rho = \rho(\mathbf{x})$ is the mass density at point $\mathbf{x}$, and $\omega = 2\pi f$ is the circular frequency. No summation over the repeated index m is assumed. In practice, the DED is estimated from the autocorrelation (power spectrum) of the recorded ambient noise wavefield and averaged over short time windows. This is equivalent to average over directions if the field is isotropic. For subsurface imaging purposes, the DED is computed from the imaginary part of the Green's function (eq. A1).

In order to demonstrate the validity of eq. (A1) and establish the proportionality factor, a simple homogeneous, isotropic, elastic medium is considered. Therefore, the analytical expression to the Green's function is known (Sánchez-Sesma *et al.* 2008).

The displacement field $u_i(\mathbf{x}, \omega)$ produced by a body force f_i at a given point $\mathbf{x}$ of an elastic solid is described by the Newton's law of displacements (eq. A2):

$$\frac{\partial}{\partial x_j}\left(c_{ijkl}\frac{\partial u_l(\mathbf{x}, \omega)}{\partial x_k}\right) + \omega^2 \rho u_i(\mathbf{x}, \omega) = -f_i(\mathbf{x}, \omega). \tag{A2}$$

Eq. (A2) is often called elastic wave equation or the Navier equation. Here c_{ijkl} is the stiffness tensor. The Einstein summation convention is assumed, that is, repeated index implies summation over the range of that index.

From eq. (A2), it is possible to derive the classical Somigliana representation theorem (e.g. van Manen *et al.* 2006; Wapenaar & Fokkema 2006; Snieder *et al.* 2007; Sánchez-Sesma *et al.* 2008, 2018)

$$u_m(\mathbf{x_A}, \omega) = \int_\Gamma [G_{im}(\mathbf{x}, \mathbf{x_A}, \omega) t_i(\mathbf{x}, \omega) - T_{im}(\mathbf{x}, \mathbf{x_A}, \omega) u_i(\mathbf{x}, \omega)]\, \mathrm{d}\Gamma_x + \int_V f_i(\mathbf{x}, \omega) G_{im}(\mathbf{x_A}, \mathbf{x}, \omega) \mathrm{d}V_x \tag{A3}$$

in which one has the displacement field for $\mathbf{x_A}$ being a point at V inside the surface Γ in terms of body forces and the boundary values of displacements and tractions. Here $G_{im}(\mathbf{x_A}, \mathbf{x}, \omega)$ and $T_{im}(\mathbf{x_A}, \mathbf{x}, \omega)$ are the Green's functions for displacements and tractions when the harmonic unit force are in the direction m. $f_i(\mathbf{x})$ is the body force distribution. $t_i(\mathbf{x}, \omega)$ and $T_{im}(\mathbf{x_A}, \mathbf{x}, \omega)$ are defined by eq. (A4):

$$\begin{aligned} t_i(\mathbf{x}, \omega) &= n_j(\mathbf{x})\left(c_{ijkl}\frac{\partial u_l(\mathbf{x}, \omega)}{\partial x_k}\right) \\ T_{im}(\mathbf{x_A}, \mathbf{x}, \omega) &= n_j(\mathbf{x})\left(c_{ijkl}\frac{\partial G_{lm}(\mathbf{x}, \mathbf{x_A}, \omega)}{\partial x_k}\right). \end{aligned} \tag{A4}$$

By considering for the internal point $\mathbf{x_B}$ an harmonic body force $f_i(\mathbf{x}) \equiv \delta(\mathbf{x} - \mathbf{x_B})\delta_{in}$ in the direction n and setting for the field the time-reversed solution, then $u_i(\mathbf{x}) \equiv G_{in}(\mathbf{x}, \mathbf{x_B}, \omega)$, $t_i(\mathbf{x}) \equiv T_{in}(\mathbf{x}, \mathbf{x_B}, \omega)$, and eq. (A3) becomes

$$\int_\Gamma \left[T_{im}(\mathbf{x}, \mathbf{x_A}, \omega) G_{in}^*(\mathbf{x}, \mathbf{x_B}, \omega) - T_{in}^*(\mathbf{x}, \mathbf{x_B}, \omega) G_{im}(\mathbf{x}, \mathbf{x_A}, \omega)\right] \mathrm{d}\Gamma_x = -G_{mn}^*(\mathbf{x_A}, \mathbf{x_B}, \omega) + G_{mn}(\mathbf{x_A}, \mathbf{x_B}, \omega), \tag{A5}$$

which is rewritten changing $\mathbf{x}$ by ξ, to represent boundary points on Γ, as

$$2\mathbf{i}G_{mn}(\mathbf{x_A}, \mathbf{x_B}, \omega) = -\int_{\Gamma} \left[G_{mi}(\mathbf{x_A}, \xi, \omega)T^*_{in}(\xi, \mathbf{x_B}, \omega) - G^*_{ni}(\mathbf{x_B}, \xi, \omega)T_{im}(\xi, \mathbf{x_A}, \omega)\right] \mathrm{d}\Gamma_{\xi}. \tag{A6}$$

Eq. (A6) is a correlation-type representation theorem. A similar form has been presented by van Manen *et al.* (2006). Then because the theorem in eq. (A6) is valid for any surface Γ, it follows that if the field is diffuse at the envelope, that is, the net flux of energy is null, it is also diffuse at any point within the heterogeneous medium

Starting from the analytical expressions for G_{im} and T_{im} in the farfield (Sánchez-Sesma & Campillo 2006; Sánchez-Sesma *et al.* 2008; see e.g. Domínguez & Abascal 1984 for the full expression of G_{im} and T_{im}), it can be demonstrated that for random and uncorrelated sources, the resulting illumination, after a lapse time large enough compared to the traveltime of ballistic waves, is an equipartitioned diffuse field. Therefore, the right-hand side of eq. (A6) is proportional to the azimuthal average of cross-correlation of the displacement field:

$$\mathrm{Im}[G_{mn}(\mathbf{x_A}, \mathbf{x_B})] = -(2\pi\xi_S)^{-1}k^3\langle u_m(\mathbf{x_A})u^*_n(\mathbf{x_B})\rangle, \tag{A7}$$

where k is the shear wave number and ξ_S is the average energy density of shear waves and represents a measure of the strength of the diffuse illumination. Assuming the source and the receiver are at the same location ($\mathbf{x_A} = \mathbf{x_B} = \mathbf{x}$), one can thus write (Sánchez-Sesma *et al.* 2008)

$$\mathrm{Im}[G_{mm}(\mathbf{x}, \mathbf{x})] = -(2\pi\xi_S)^{-1}k^3\langle|u_m(\mathbf{x})|^2\rangle. \tag{A8}$$

An alternative approach linking the azimuthal average of cross-correlation to the imaginary part of the Green's function under diffuse assumption in the farfield and without prior knowledge of the full analytical expression of the Green's function was presented by Snieder *et al.* (2009).

APPENDIX B: ESTIMATING THE *SH* WAVES CONTRIBUTION TO THE IMAGINARY PART OF THE GREEN'S FUNCTION

B1 Receiver at the surface

Following Aki & Richards (2002), and for the displacement $u_2 = v$, the *SH*-wave equation in an arbitrary layer j presented in Fig. 1 is given in linear elasticity by

$$\frac{\partial^2 v}{\partial t^2} = \frac{\mu_j}{\rho_j}\left(\frac{\partial^2 v}{\partial x^2} + \frac{\partial^2 v}{\partial z^2}\right). \tag{B1}$$

A solution to eq. (B1) can be of the form

$$v = l_1(z, w, k)\exp[i(kx - \omega t)] \tag{B2}$$

and the associated shear stresses:

$$\begin{aligned}\tau_{yz} &= \mu_j\frac{\partial l_1}{\partial z}\exp[i(kx - \omega t)]\\ &= l_2\exp[i(kx - \omega t)]\\ \tau_{xy} &= ik\mu_j l_1\exp[i(kx - \omega t)].\end{aligned} \tag{B3}$$

From eq. (B3), the differential eq. (B4) is obtained:

$$\frac{\mathrm{d}l_1}{\mathrm{d}z} = \frac{1}{\mu_j}l_2 \tag{B4}$$

From Newton's second law, one gets

$$\frac{\partial\tau_{xy}}{\partial x} + \frac{\partial\tau_{yz}}{\partial z} = \rho_j\frac{\partial^2 v}{\partial t^2}. \tag{B5}$$

This leads to

$$\frac{\mathrm{d}l_2}{\mathrm{d}z} = (k^2\mu_j - \omega^2\rho_j)l_1. \tag{B6}$$

Eqs (B4) and (B6) lead to the system of first-order differential eq. (B7):

$$\frac{\mathrm{d}}{\mathrm{d}z}\begin{pmatrix}l_1\\ l_2\end{pmatrix} = \begin{pmatrix}0 & \frac{1}{\mu_j}\\ k^2\mu_j - \omega^2\rho_j & 0\end{pmatrix}\begin{pmatrix}l_1\\ l_2\end{pmatrix}. \tag{B7}$$

This equation is of the form

$$\frac{\mathrm{d}\mathbf{l}}{\mathrm{d}z} = \mathbf{A}_j\mathbf{l}, \tag{B8}$$

where

$$\mathbf{l} = \begin{pmatrix} l_1 \\ l_2 \end{pmatrix} \tag{B9}$$

and

$$\mathbf{A}_j = \begin{pmatrix} 0 & \frac{1}{\mu_j} \\ k^2\mu_j - \omega^2\rho_j & 0 \end{pmatrix}. \tag{B10}$$

Assuming a homogeneous layer medium (i.e. the layers' properties are constant), the solution to eq. (B8) within the *j*th layer defined by z_j and z_{j+1} is given by

$$\begin{pmatrix} l_1 \\ l_2 \end{pmatrix}_{z_{j+1}} = \mathbf{P}_j \begin{pmatrix} l_1 \\ l_2 \end{pmatrix}_{z_j}, \tag{B11}$$

where

$$\mathbf{P}_j = \exp[\mathbf{A}_j(z_{j+1} - z_j)]. \tag{B12}$$

Using linear algebra properties, it can be shown that if matrix $\mathbf{A}$ is diagonalizable, then there exists an invertible $\mathbf{L}$ so that

$$\mathbf{A} = \mathbf{L}\mathbf{e}\mathbf{L}^{-1} \tag{B13}$$

where $\mathbf{L}$ is the matrix of eigenvectors of $\mathbf{A}$, $\mathbf{L}^{-1}$ its inverse and $\mathbf{e}$ is the eigenvalue matrix. The series expansion of $\exp[\mathbf{A}(z_{j+1} - z_j)]$ using

$$\exp(\mathbf{A}) = \sum_{k=0}^{\infty} \frac{\mathbf{A}^k}{k!} = \mathbf{I} + \mathbf{A} + \frac{\mathbf{A}^2}{2!} + \frac{\mathbf{A}^3}{3!} + \cdots \tag{B14}$$

allows to write

$$\exp(\mathbf{L}^{-1}\mathbf{A}\mathbf{L}) = \exp(\mathbf{e}) = \mathbf{E} = \mathbf{L}^{-1}\left(\mathbf{I} + \mathbf{A} + \frac{\mathbf{A}^2}{2!} + \frac{\mathbf{A}^3}{3!} + \ldots\right)\mathbf{L} = \mathbf{L}^{-1}[\exp(\mathbf{A})]\mathbf{L}, \tag{B15}$$

where $\mathbf{E} = \exp(\mathbf{e})$. For the problem investigated, $\mathbf{A}$ is replaced by $\mathbf{A}_j(z_{j+1} - z_j)$.

The eigenvalues for the 2×2 $\mathbf{A}(z_{j+1} - z_j)$ for the *SH* wave propagation are obtained by finding the roots of the second-order polynomial defined by

$$\det[\mathbf{A}_j(z_{j+1} - z_j) - \lambda I] = 0. \tag{B16}$$

This leads to

$$\lambda_1 = (z_{j+1} - z_j)\nu_j \tag{B17}$$

$$\lambda_2 = -(z_{j+1} - z_j)\nu_j \tag{B18}$$

where $\nu_j = \sqrt{k^2 - \frac{\omega^2\rho_j}{\mu_j}} = \sqrt{k^2 - \frac{\omega^2}{V_{S_j}^2}}$.

The eigenvectors are obtained by solving the equations (for the two eigenvalues)

$$[\mathbf{A}_j(z_{j+1} - z_j) - \lambda_1 I]\begin{pmatrix} x_1 \\ x_2 \end{pmatrix} = 0 \tag{B19}$$

and

$$[\mathbf{A}_j(z_{j+1} - z_j) - \lambda_2 I]\begin{pmatrix} x_1 \\ x_2 \end{pmatrix} = 0. \tag{B20}$$

Sample eigenvectors are therefore:

for λ_1:

$$(x_1, x_2) = (1, \mu_j\nu_j)x_1 \tag{B21}$$

and for λ_2:

$$(x_1, x_2) = (1, -\mu_j\nu_j)x_1. \tag{B22}$$

The eigenvectors can be arranged in the matrix

$$\mathbf{L}_j = \begin{pmatrix} 1 & 1 \\ \mu_j\nu_j & -\mu_j\nu_j \end{pmatrix} \tag{B23}$$

and the inverse of $\mathbf{L}_j$ is given by

$$\mathbf{L}_j^{-1} = \begin{pmatrix} \frac{1}{2} & \frac{1}{2\mu_j \nu_j} \\ \frac{1}{2} & \frac{-1}{2\mu_j \nu_j} \end{pmatrix}. \tag{B24}$$

Matrix $\mathbf{E}_j$ is given by

$$\mathbf{E}_j = \begin{pmatrix} \exp[\nu_j(z_{j+1} - z_j)] & 0 \\ 0 & \exp[-\nu_j(z_{j+1} - z_j)] \end{pmatrix}. \tag{B25}$$

The eigenvalue problem has also been studied by Gantmacher (1959) and Gilbert & Backus (1966).

The propagator (or layer) matrix can therefore be written as

$$\begin{aligned} \mathbf{P}_j &= \mathbf{L}_j \mathbf{E}_j \mathbf{L}_j^{-1} \\ &= \begin{pmatrix} 1 & 1 \\ \mu_j \nu_j & -\mu_j \nu_j \end{pmatrix} \begin{pmatrix} \exp[\nu_j(z_{j+1} - z_j)] & 0 \\ 0 & \exp[-\nu_j(z_{j+1} - z_j)] \end{pmatrix} \begin{pmatrix} \frac{1}{2} & \frac{1}{2\mu_j \nu_j} \\ \frac{1}{2} & \frac{-1}{2\mu_j \nu_j} \end{pmatrix}. \end{aligned} \tag{B26}$$

This operation leads to

$$\mathbf{P}_j = \begin{pmatrix} \cosh[\nu_j(z_{j+1} - z_j)] & \frac{1}{\mu_j \nu_j} \sinh[\nu_j(z_{j+1} - z_j)] \\ \mu_j \nu_j \sinh[\nu_j(z_{j+1} - z_j)] & \cosh[\nu_j(z_{j+1} - z_j)] \end{pmatrix}. \tag{B27}$$

In the next steps, the propagator matrix as defined by eq. (B26) is used. This representation allows to introduce a manipulation matrix that aids to avoid the numerical instability issue.

For an n-layer over half-space system, we obtain

$$\begin{pmatrix} l_1 \\ l_2 \end{pmatrix}_{z_{n+1}} = \mathbf{P}_n \mathbf{P}_{n-1} \ldots \mathbf{P}_1 \begin{pmatrix} l_1 \\ l_2 \end{pmatrix}_{z_1}. \tag{B28}$$

By introducing eq. (B2) into eq. (B5), a second-order differential equation is obtained for l_1 where the solution can be written for layer 1 in the form

$$l_1 = \acute{S}_1 \exp(\nu_1 z) + \grave{S}_1 \exp(-\nu_1 z), \tag{B29}$$

where $\acute{S}_1$ and $\grave{S}_1$ are constant representing the amplitude of upgoing and downgoing *SH* waves.

Eqs (B4) and (B29) lead to

$$l_2 = \mu_1 \nu_1 \acute{S}_1 \exp(\nu_1 z) - \mu_1 \nu_1 \grave{S}_1 \exp(-\nu_1 z). \tag{B30}$$

Eqs (B29) and (B30) combine to

$$\begin{pmatrix} l_1 \\ l_2 \end{pmatrix} = \begin{pmatrix} \exp(\nu_1 z) & \exp(-\nu_1 z) \\ \mu_1 \nu_1 \exp(\nu_1 z) & -\mu_1 \nu_1 \exp(-\nu_1 z) \end{pmatrix} \begin{pmatrix} \acute{S}_1 \\ \grave{S}_1 \end{pmatrix}. \tag{B31}$$

Without loss of generality, we have for the half-space:

$$\begin{aligned} \begin{pmatrix} l_1 \\ l_2 \end{pmatrix}_{n+1} &= \begin{pmatrix} \exp(\nu_{n+1} z) & \exp(-\nu_{n+1} z) \\ \mu_{n+1} \nu_{n+1} \exp(\nu_{n+1} z) & -\mu_{n+1} \nu_{n+1} \exp(-\nu_{n+1} z) \end{pmatrix} \begin{pmatrix} \acute{S}_{n+1} \\ \grave{S}_{n+1} \end{pmatrix} \\ &= \begin{pmatrix} 1 & 1 \\ \mu_{n+1} \nu_{n+1} & -\mu_{n+1} \nu_{n+1} \end{pmatrix} \begin{pmatrix} \acute{S}_1 \exp(\nu_{n+1} z) \\ \grave{S}_1 \exp(-\nu_{n+1} z) \end{pmatrix} \\ &= \mathbf{L}_{n+1} \begin{pmatrix} \acute{S}_{n+1} \exp(\nu_{n+1} z) \\ \grave{S}_{n+1} \exp(-\nu_{n+1} z) \end{pmatrix} \\ &= \mathbf{L}_{n+1} \begin{pmatrix} \exp(\nu_{n+1} z_{n+1}) & 0 \\ 0 & \exp(-\nu_{n+1} z_{n+1}) \end{pmatrix} \begin{pmatrix} \acute{S}_{n+1} \\ \grave{S}_{n+1} \end{pmatrix}. \end{aligned} \tag{B32}$$

In the half-space, there is no upgoing waves, therefore $\acute{S}_{n+1} = 0$, so that

$$\begin{aligned} \begin{pmatrix} l_1 \\ l_2 \end{pmatrix}_{n+1} &= \mathbf{L}_{n+1} \begin{pmatrix} \exp(\nu_{n+1} z_{n+1}) & 0 \\ 0 & \exp(-\nu_{n+1} z_{n+1}) \end{pmatrix} \begin{pmatrix} 0 \\ \grave{S}_{n+1} \end{pmatrix} \\ &= \mathbf{L}_{n+1} \begin{pmatrix} \exp(\nu_{n+1} z_{n+1}) & 0 \\ 0 & \exp(-\nu_{n+1} z_{n+1}) \end{pmatrix} \begin{pmatrix} 0 \\ 1 \end{pmatrix} \grave{S}_{n+1}. \end{aligned} \tag{B33}$$

Using eqs (B26), (B28) and (B33), we have

$$\mathbf{P}_n\mathbf{P}_{n-1}...\mathbf{P}_1\begin{pmatrix} l_1 \\ l_2 \end{pmatrix}_1 = \mathbf{L}_{n+1}\begin{pmatrix} \exp(\nu_{n+1}z_{n+1}) & 0 \\ 0 & \exp(-\nu_{n+1}z_{n+1}) \end{pmatrix}\begin{pmatrix} 0 \\ 1 \end{pmatrix}\dot{S}_{n+1}. \tag{B34}$$

This leads, for the displacement at the surface, to

$$\begin{pmatrix} l_1 \\ l_2 \end{pmatrix}_1 = \mathbf{P}_1^{-1}...\mathbf{P}_{n-1}^{-1}\mathbf{P}_n^{-1}\mathbf{L}_{n+1}\begin{pmatrix} 0 \\ 1 \end{pmatrix}\dot{S}_{n+1}\exp(-\nu_{n+1}z_{n+1}), \tag{B35}$$

where $\mathbf{P}_n^{-1} = \mathbf{L}_n\mathbf{E}_n^{-1}\mathbf{L}_n^{-1}$.

Let set $\mathbf{C}_{n+1} = \begin{pmatrix} 0 \\ 1 \end{pmatrix}$ and $\mathbf{Y}_{n+1} = \mathbf{L}_{n+1}\mathbf{C}_{n+1}$.

At the surface load point ($z = 0$), $l_1 = v = g_{22\mathrm{SH}}$ (the integrand of interest) and $l_2 = 1$.

Eq. (B35) can be solved for $g_{22\mathrm{SH}}$ at the surface.

The Green's function in the 1-D layered medium is obtained by integration over the horizontal wavenumber:

$$\mathrm{Im}\left[G_{22}^{SH}(z, f)\right] = \mathrm{Im}\left[G_{11}^{SH}(z, f)\right] = \frac{1}{4\pi}\int_0^\infty \mathrm{Im}\left[g_{22\mathrm{SH}}\right]k\mathrm{d}k \tag{B36}$$

Note that a correction factor $\frac{k}{4\pi}$ has been introduced in the kernel. This is trivial in cylindrical coordinates when the radius and azimuthal components are set to zero.

B2 Receiver at depth

For a receiver at depth, the displacement stress just under the load point which is assumed to be at the interface j can be written as follows (compare eq. B35):

$$\begin{pmatrix} l_{b1} \\ l_{b2} \end{pmatrix}_{z_j} = \mathbf{P}_j^{-1}...\mathbf{P}_{n-1}^{-1}\mathbf{P}_n^{-1}\mathbf{L}_{n+1}\begin{pmatrix} 0 \\ 1 \end{pmatrix}\dot{S}_{n+1}\exp(-\nu_{n+1}z_{n+1}). \tag{B37}$$

On the other hand, the result just above the source would be

$$\begin{pmatrix} l_{u1} \\ l_{u2} \end{pmatrix}_{z_j} = \mathbf{P}_{j-1}\mathbf{P}_{j-2}...\mathbf{P}_1\begin{pmatrix} l_1 \\ l_2 \end{pmatrix}_{z_1}. \tag{B38}$$

The boundary conditions at the load point at depth are given (1) for the upper layer by $l_{u1} = g_{22\mathrm{SH}}$; and $l_{u2} = \tau_u$ and (2) for the bottom layers by $l_{b1} = g_{22\mathrm{SH}}$ and $l_{b2} = \tau_b$. The unit load at the source is defined such that $\tau_b - \tau_u = 1$

Eq. (B38) can be rewritten as

$$\begin{aligned} \begin{pmatrix} l_{u1} \\ l_{u2} \end{pmatrix}_{z_j} &= \mathbf{P}_{j-1}\mathbf{P}_{j-2}...\mathbf{P}_1\begin{pmatrix} v_s \\ 0 \end{pmatrix}_{z_1} \\ &= \mathbf{P}_{j-1}\mathbf{P}_{j-2}...\mathbf{P}_1\begin{pmatrix} 1 \\ 0 \end{pmatrix}v_s. \end{aligned} \tag{B39}$$

Let set $\mathbf{Y}_1 = \begin{pmatrix} 1 \\ 0 \end{pmatrix}$ as the basic displacement-stress solution at the surface. This basic vector is propagated downwards from the surface to the source. So that

$$\begin{pmatrix} Y_{u1} \\ Y_{u2} \end{pmatrix} = \mathbf{P}_{j-1}\mathbf{P}_{j-2}...\mathbf{P}_1\begin{pmatrix} 1 \\ 0 \end{pmatrix}. \tag{B40}$$

Respectively, the fundamental vector of plane-wave amplitude $\begin{pmatrix} 0 \\ 1 \end{pmatrix}$ at the half-space can be propagated upwards to the source:

$$\begin{pmatrix} Y_{b1} \\ Y_{b2} \end{pmatrix} = \mathbf{P}_j^{-1}...\mathbf{P}_{n-1}^{-1}\mathbf{P}_n^{-1}\mathbf{L}_{n+1}\begin{pmatrix} 0 \\ 1 \end{pmatrix}. \tag{B41}$$

The set of boundary conditions allows to extract $g_{22\mathrm{SH}}$ as

$$g_{22\mathrm{SH}} = \frac{Y_{u1}Y_{b1}}{Y_{u1}Y_{b2} - Y_{u2}Y_{b1}}. \tag{B42}$$

For this *SH* case, the Green's function in the 1-D layered medium is given by

$$\mathrm{Im}\left[G_{22}^{SH}(z, f)\right] = \mathrm{Im}\left[G_{11}^{SH}(z, f)\right] = \frac{1}{4\pi}\int_0^\infty \mathrm{Im}\left[g_{22\mathrm{SH}}\right]k\mathrm{d}k. \tag{B43}$$

The integral can be numerically computed by making, for example, use of the discrete wavenumber approach.

APPENDIX C: COMPUTING THE *P–SV* WAVES CONTRIBUTION TO THE IMAGINARY PART OF THE GREEN'S FUNCTION

Without loss of generality, consider the inplane solution (i.e. no dependence on the y coordinate) to the elastic wave or Navier equation. The displacement-stress vector $\mathbf{r} = (r_1, r_2, r_3, r_4)^T$ is obtained by the following expression (see also e.g. Aki & Richards 2002,Chap7, p263):

$$\begin{aligned} u &= r_1(k, z, \omega)\exp[i(kx - \omega t)], \\ v &= 0, \\ w &= ir_2(k, z, \omega)\exp[i(kx - \omega t)]. \end{aligned} \tag{C1}$$

Here we used $(u_1, u_2, u_3) = (u, v, w)$. Let set the stresses associated with displacements:

$$\begin{aligned} \tau_{zx} &= r_3(k, z, \omega)\exp[i(kx - \omega t)], \\ \tau_{zz} &= ir_4(k, z, \omega)\exp[i(kx - \omega t)]. \end{aligned} \tag{C2}$$

Using Hooke's and Newton's law for a homogeneous medium it can be shown that

$$\frac{\mathrm{d}}{\mathrm{d}z}\begin{pmatrix} r_1 \\ r_2 \\ r_3 \\ r_4 \end{pmatrix} = \begin{pmatrix} 0 & k & \frac{1}{\mu} & 0 \\ \frac{-k\lambda}{\lambda+2\mu} & 0 & 0 & \frac{1}{\lambda+2\mu} \\ \frac{4k^2\mu(\lambda+\mu)}{\lambda+2\mu} - \omega^2\rho & 0 & 0 & \frac{k\lambda}{\lambda+2\mu} \\ 0 & -\omega^2\rho & -k & 0 \end{pmatrix}\begin{pmatrix} r_1 \\ r_2 \\ r_3 \\ r_4 \end{pmatrix}, \tag{C3}$$

which is the first-order differential equation for displacement-stress vector $\mathbf{r}$. λ and ν are the Lamé parameters.

Assuming a layer homogeneous medium (i.e. the layers' properties do not depend on the depth z for a given layer), the solution to eq. (C3) at two points z_1 and z_2 is given by

$$\begin{pmatrix} r_1 \\ r_2 \\ r_3 \\ r_4 \end{pmatrix}_{z_2} = \mathbf{P}\begin{pmatrix} r_1 \\ r_2 \\ r_3 \\ r_4 \end{pmatrix}_{z_1} \tag{C4}$$

where

$$\mathbf{P} = \exp[\mathbf{A}(z_2 - z_1)] \tag{C5}$$

and

$$\mathbf{A} = \begin{pmatrix} 0 & k & \frac{1}{\mu} & 0 \\ \frac{-k\lambda}{\lambda+2\mu} & 0 & 0 & \frac{1}{\lambda+2\mu} \\ \frac{4k^2\mu(\lambda+\mu)}{\lambda+2\mu} - \omega^2\rho & 0 & 0 & \frac{k\lambda}{\lambda+2\mu} \\ 0 & -\omega^2\rho & -k & 0 \end{pmatrix}. \tag{C6}$$

The eigenvalues for the 4×4 matrix $\mathbf{A}(z_2 - z_1)$ for the *P–SV* wave propagation are obtained by finding the roots of the fourth-order polynomial defined by:

$$\det[\mathbf{A}(z_2 - z_1) - a\mathbf{I}] = 0. \tag{C7}$$

This leads to

$$\begin{aligned} a_1 &= \gamma = \sqrt{k^2 - \frac{\omega^2}{\alpha}}(z_2 - z_1) \\ a_2 &= \nu = \sqrt{k^2 - \frac{\omega^2}{\beta}}(z_2 - z_1) \\ a_3 &= -\gamma = -\sqrt{k^2 - \frac{\omega^2}{\alpha}}(z_2 - z_1) \\ a_4 &= -\nu = -\sqrt{k^2 - \frac{\omega^2}{\beta}}(z_2 - z_1), \end{aligned} \tag{C8}$$

α and V_p and β and V_s are used interchangeably.

Using linear algebra properties as presented in eqs (B13)–(B15), we obtain

$$\mathbf{L} = \begin{pmatrix} \alpha k & \beta \nu & \alpha k & \beta \nu \\ \alpha \gamma & \beta k & -\alpha \gamma & -\beta k \\ -2\alpha\mu k\gamma & -\beta\mu(k^2+\nu^2) & 2\alpha\mu k\gamma & \beta\mu(k^2+\nu^2) \\ -\alpha\mu(k^2+\nu^2) & -2\beta\mu k\nu & -\alpha\mu(k^2+\nu^2) & -2\beta\mu k\nu \end{pmatrix} \tag{C9}$$

$$\mathbf{E} = \begin{pmatrix} \exp\left[\gamma(z_2-z_1)\right] & 0 & 0 & 0 \\ 0 & \exp\left[\nu(z_2-z_1)\right] & 0 & 0 \\ 0 & 0 & \exp\left[-\gamma(z_2-z_1)\right] & 0 \\ 0 & 0 & 0 & \exp\left[-\nu(z_2-z_1)\right] \end{pmatrix} \tag{C10}$$

$$\mathbf{L}^{-1} = \frac{\beta}{2\alpha\mu\gamma\nu\omega^2} \begin{pmatrix} 2\beta\mu k\gamma\nu & -\beta\mu\nu(k^2+\nu^2) & -\beta k\nu & \beta\gamma\nu \\ -\alpha\mu\gamma(k^2+\nu^2) & 2\alpha\mu k\gamma\nu & \alpha\gamma\nu & -\alpha k\gamma \\ 2\beta\mu k\gamma\nu & \beta\mu\nu(k^2+\nu^2) & \beta k\nu & -\beta\gamma\nu \\ -\alpha\mu\gamma(k^2+\nu^2) & -2\alpha\mu k\gamma\nu & -\alpha\gamma\nu & -\alpha k\gamma \end{pmatrix}, \tag{C11}$$

where $\mathbf{L}$, $\mathbf{E}$ are the corresponding eigenvector and exponential of the eigenvalue matrices, respectively.

Eq. (C4) can be rewritten as

$$\begin{pmatrix} r_1 \\ r_2 \\ r_3 \\ r_4 \end{pmatrix}_{z_2} = \mathbf{P} \begin{pmatrix} r_1 \\ r_2 \\ r_3 \\ r_4 \end{pmatrix}_{z_1} = \mathbf{L}\mathbf{E}\mathbf{L}^{-1} \begin{pmatrix} r_1 \\ r_2 \\ r_3 \\ r_4 \end{pmatrix}_{z_1}. \tag{C12}$$

Without loss of generality, for the elastic layer n with layer top labelled n, the displacement-stress vector at the bottom interface labelled $n+1$ is given by

$$\begin{pmatrix} r_1 \\ r_2 \\ r_3 \\ r_4 \end{pmatrix}_{z_{n+1}} = \mathbf{P}_n \begin{pmatrix} r_1 \\ r_2 \\ r_3 \\ r_4 \end{pmatrix}_{z_n} \tag{C13}$$

where

$$\mathbf{P}_n = \mathbf{L}_n \mathbf{E}_n \mathbf{L}_n^{-1}. \tag{C14}$$

For an n-layer over half-space earth model, we obtain

$$\begin{pmatrix} r_1 \\ r_2 \\ r_3 \\ r_4 \end{pmatrix}_{z_{n+1}} = \mathbf{P}_n \mathbf{P}_{n-1} \ldots \mathbf{P}_1 \begin{pmatrix} r_1 \\ r_2 \\ r_3 \\ r_4 \end{pmatrix}_{z_1}. \tag{C15}$$

It can also be shown that

$$\begin{pmatrix} r_1 \\ r_2 \\ r_3 \\ r_4 \end{pmatrix}_{n+1} = \mathbf{L}_{n+1} \begin{pmatrix} \exp(\gamma_{n+1} z_{n+1}) & 0 & 0 & 0 \\ 0 & \exp(\nu_{n+1} z_{n+1}) & 0 & 0 \\ 0 & 0 & \exp(-\gamma_{n+1} z_{n+1}) & 0 \\ 0 & 0 & 0 & \exp(-\nu_{n+1} z_{n+1}) \end{pmatrix} \begin{pmatrix} \dot{P}_{n+1} \\ \dot{S}_{n+1} \\ \dot{P}_{n+1} \\ \dot{S}_{n+1} \end{pmatrix}. \tag{C16}$$

In the half-space, there is no upgoing P and SV waves, therefore $\acute{P}_{n+1} = 0$ and $\acute{S}_{n+1} = 0$:

$$\begin{pmatrix} r_1 \\ r_2 \\ r_3 \\ r_4 \end{pmatrix}_{n+1} =$$

$$\mathbf{L}_{n+1} \begin{pmatrix} \exp(\gamma_{n+1} z_{n+1}) & 0 & 0 & 0 \\ 0 & \exp(\nu_{n+1} z_{n+1}) & 0 & 0 \\ 0 & 0 & \exp(-\gamma_{n+1} z_{n+1}) & 0 \\ 0 & 0 & 0 & \exp(-\mu_{n+1} z_{n+1}) \end{pmatrix} \begin{pmatrix} 0 \\ 0 \\ \grave{P}_{n+1} \\ \grave{S}_{n+1} \end{pmatrix}. \tag{C17}$$

$$= \mathbf{L}_{n+1} \begin{pmatrix} 0 & 0 \\ 0 & 0 \\ 1 & 0 \\ 0 & 1 \end{pmatrix} \begin{pmatrix} \grave{P}_{n+1} \exp(-\gamma_{n+1} z_{n+1}) \\ \grave{S}_{n+1} \exp(-\mu_{n+1} z_{n+1}) \end{pmatrix}$$

The later representation together with the defined manipulation matrix (Appendix D) allows to propagate the orthonormal base vectors $(0, 0, 1, 0)^T$ and $(0, 0, 0, 1)^T$, that is, the 2×1 matrix in an efficient way and ultimately to avoid the loss of precision issue associated with the Thomson–Haskell propagator matrix. See also Wang (1999).

C1 Receiver at the surface

Harmonic horizontal load: for a receiver at the surface, the boundary conditions for a harmonic horizontal load are the following:

$$\begin{pmatrix} r_1 \\ r_2 \\ r_3 \\ r_4 \end{pmatrix}_1 = \begin{pmatrix} g_{11\mathrm{PSV}} \\ g_{31\mathrm{PSV}}/i \\ -1 \\ 0 \end{pmatrix}. \tag{C18}$$

Harmonic vertical load: for a receiver at the surface, the boundary conditions for a harmonic vertical load are the following:

$$\begin{pmatrix} r_1 \\ r_2 \\ r_3 \\ r_4 \end{pmatrix}_1 = \begin{pmatrix} g_{13\mathrm{PSV}} \\ g_{33\mathrm{PSV}}/i \\ 0 \\ -1/i \end{pmatrix}. \tag{C19}$$

In the half-space, we have the following boundary conditions:

$$\begin{pmatrix} \grave{P} \\ \grave{S} \\ \acute{P} \\ \acute{S} \end{pmatrix} = \begin{pmatrix} \grave{P} \\ \grave{S} \\ 0 \\ 0 \end{pmatrix}. \tag{C20}$$

For the harmonic horizontal load we then have

$$\begin{pmatrix} \grave{P} \\ \grave{S} \\ 0 \\ 0 \end{pmatrix} = \mathbf{L_{n+1}}^{-1} \mathbf{P}_n \mathbf{P}_{n-1} \ldots \mathbf{P}_1 \begin{pmatrix} g_{11\mathrm{PSV}} \\ g_{31\mathrm{PSV}}/i \\ -1 \\ 0 \end{pmatrix} \tag{C21}$$

and for the harmonic vertical load

$$\begin{pmatrix} \grave{P} \\ \grave{S} \\ 0 \\ 0 \end{pmatrix} = \mathbf{L_{n+1}}^{-1} \mathbf{P}_n \mathbf{P}_{n-1} \ldots \mathbf{P}_1 \begin{pmatrix} g_{13\mathrm{PSV}} \\ g_{33\mathrm{PSV}}/i \\ 0 \\ -1/i \end{pmatrix}. \tag{C22}$$

The two equations above can be solved for $g_{11\mathrm{PSV}}$ and $g_{33\mathrm{PSV}}$.

The Green's function for the P–SV case in a 1-D layered medium are then given by

$$\mathrm{Im}\left[G_{22}^{\text{P-SV}}(z, f)\right] = \mathrm{Im}\left[G_{11}^{\text{P-SV}}(z, f)\right] = \frac{1}{4\pi} \int_0^\infty \mathrm{Im}\left[g_{11\mathrm{PSV}}\right] k \mathrm{d}k \tag{C23}$$

$$\mathrm{Im}\left[G_{33}^{\text{P-SV}}(z_F, f)\right] = \frac{1}{2\pi} \int_0^\infty \mathrm{Im}\left[g_{33\mathrm{PSV}}\right] k \mathrm{d}k. \tag{C24}$$

C2 Receiver at depth

The displacement-stress vector from the half-space to the source/receiver can be written in terms of the amplitudes of the waves in the half-space as

$$\mathbf{L}_{n+1}\begin{pmatrix}0&0\\0&0\\1&0\\0&1\end{pmatrix}\begin{pmatrix}\dot{P}\\\dot{S}\end{pmatrix}=\begin{pmatrix}r_1\\r_2\\r_3\\r_4\end{pmatrix}_{n+1}=\mathbf{P}_n\mathbf{P}_{n-1}\ldots\mathbf{P}_j\begin{pmatrix}r_{b1}\\r_{b2}\\r_{b3}\\r_{b4}\end{pmatrix}_j \tag{C25}$$

or

$$\begin{pmatrix}r_{b1}\\r_{b2}\\r_{b3}\\r_{b4}\end{pmatrix}_j=\mathbf{P}_j^{-1}\ldots\mathbf{P}_{n-1}^{-1}\mathbf{P}_n^{-1}\mathbf{L}_{n+1}\begin{pmatrix}0&0\\0&0\\1&0\\0&1\end{pmatrix}\begin{pmatrix}\dot{P}\\\dot{S}\end{pmatrix}. \tag{C26}$$

The displacement-stress vector from the free surface to the source/receiver are linked by

$$\begin{pmatrix}r_{u1}\\r_{u2}\\r_{u3}\\r_{u4}\end{pmatrix}_j=\mathbf{P}_j\mathbf{P}_{j-1}\ldots\mathbf{P}_1\begin{pmatrix}1&0\\0&1\\0&0\\0&0\end{pmatrix}\begin{pmatrix}u\\w\end{pmatrix}. \tag{C27}$$

The propagation of the fundamental independent solutions of the displacement stress at the surface down to the source can be defined as the columns of

$$\begin{pmatrix}Y_{u11}&Y_{u12}\\Y_{u21}&Y_{u22}\\Y_{u31}&Y_{u32}\\Y_{u41}&Y_{u42}\end{pmatrix}=\mathbf{P}_{j-1}\mathbf{P}_{j-2}\ldots\mathbf{P}_1\begin{pmatrix}1&0\\0&1\\0&0\\0&0\end{pmatrix}. \tag{C28}$$

Similarly, the motion displacement stress just below the source compatible with unitary downgoing P and S waves at half-space are the columns of

$$\begin{pmatrix}Y_{b11}&Y_{b12}\\Y_{b21}&Y_{b22}\\Y_{b31}&Y_{b32}\\Y_{b41}&Y_{b42}\end{pmatrix}=\mathbf{P}_j^{-1}\ldots\mathbf{P}_{n-1}^{-1}\mathbf{P}_n^{-1}\mathbf{L}_{n+1}\begin{pmatrix}0&0\\0&0\\1&0\\0&1\end{pmatrix}. \tag{C29}$$

For a horizontal harmonic load, the displacements are assumed to be continuous at the source. The solution above and below the source are respectively

$$\begin{pmatrix}r_{u1}\\r_{u2}\\r_{u3}\\r_{u4}\end{pmatrix}_z=\begin{pmatrix}g_{11\mathrm{PSV}}\\g_{31\mathrm{PSV}}/i\\\sigma_{uh}\\0\end{pmatrix} \tag{C30}$$

and

$$\begin{pmatrix}r_{b1}\\r_{b2}\\r_{b3}\\r_{b4}\end{pmatrix}_z=\begin{pmatrix}g_{11\mathrm{PSV}}\\g_{31\mathrm{PSV}}/i\\\sigma_{bh}\\0\end{pmatrix}. \tag{C31}$$

The continuity of the stresses leads to the following boundary conditions:

$$\begin{aligned}&r_{u4}-r_{b4}=0\\&\sigma_{bh}-\sigma_{uh}=r_{b3}-r_{u3}=1.\end{aligned} \tag{C32}$$

The first two equations above can be written as

$$\mathbf{Ax}=\mathbf{b}_h \tag{C33}$$

where

$$\mathbf{A} = (\mathbf{Y}_b, -\mathbf{Y}_u) = \begin{pmatrix} Y_{b11} & Y_{b12} & -Y_{u11} & -Y_{u12} \\ Y_{b21} & Y_{b22} & -Y_{u21} & -Y_{u22} \\ Y_{b31} & Y_{b32} & -Y_{u31} & -Y_{u32} \\ Y_{b41} & Y_{b42} & -Y_{u41} & -Y_{u42} \end{pmatrix}, \tag{C34}$$

$$\mathbf{x} = \begin{pmatrix} \grave{P} \\ \grave{S} \\ u \\ w \end{pmatrix} \tag{C35}$$

and

$$\mathbf{b}_h = \begin{pmatrix} 0 \\ 1 \\ 0 \\ 0 \end{pmatrix}. \tag{C36}$$

Similarly, for a vertical harmonic load (upper layer at load) it follows that

$$\begin{pmatrix} r_{u1} \\ r_{u2} \\ r_{u3} \\ r_{u4} \end{pmatrix}_z = \begin{pmatrix} g_{13\mathrm{PSV}} \\ g_{33\mathrm{PSV}}/i \\ 0 \\ \sigma_{uv}/i \end{pmatrix} \tag{C37}$$

and

$$\begin{pmatrix} r_{b1} \\ r_{b2} \\ r_{b3} \\ r_{b4} \end{pmatrix}_z = \begin{pmatrix} g_{13\mathrm{PSV}} \\ g_{33\mathrm{PSV}}/i \\ 0 \\ \sigma_{bv}/i \end{pmatrix}. \tag{C38}$$

In this case, the boundary conditions are

$$\begin{aligned} r_{u4} - r_{b4} &= 1 \\ \sigma_{bv} - \sigma_{uv} = r_{b3} - r_{u3} &= 0 \\ r_{u1} = r_{b1} &= g_{13\mathrm{PSV}} \\ r_{u2} = r_{b2} &= g_{33\mathrm{PSV}}. \end{aligned} \tag{C39}$$

From the first two equations, it is possible to write, as for the horizontal load,

$$\mathbf{A}\mathbf{x} = \mathbf{b}_v \tag{C40}$$

where $\mathbf{A}$ and $\mathbf{x}$ have been defined above. $\mathbf{b}_v$ is defined in this case by

$$\mathbf{b}_v = \begin{pmatrix} 1 \\ 0 \\ 0 \\ 0 \end{pmatrix}. \tag{C41}$$

Eqs (C33) and (C40) can be solved for $g_{11\mathrm{PSV}}$ and $g_{33\mathrm{PSV}}$ by using, for example, the Gaussian LU matrix decomposition.

The Green's function in 1-D layered medium are then given by

$$\mathrm{Im}\left[G_{22}^{\text{P-SV}}(z, f)\right] = \mathrm{Im}\left[G_{11}^{\text{P-SV}}(z, f)\right] = \frac{1}{4\pi}\int_0^\infty \mathrm{Im}\left[g_{11\mathrm{PSV}}\right] k\mathrm{d}k \tag{C42}$$

$$\mathrm{Im}\left[G_{33}^{\text{P-SV}}(z_F, f)\right] = \frac{1}{2\pi}\int_0^\infty \mathrm{Im}\left[g_{33\mathrm{PSV}}\right] k\mathrm{d}k. \tag{C43}$$

The solution to the integral can be obtained numerically by using, for example, the discrete wavenumber approach.

APPENDIX D: ORTHONORMALIZATION ALGORITHM FOR THE *P–SV* WAVES PROPAGATION

D1 Propagation from the surface to the source

Starting from the definition of the base vector $\mathbf{Y}_j$ at the layer interface j (Appendix C),

$$\mathbf{Y}_{j+1} = \mathbf{P}_j\mathbf{Y}_j = \mathbf{L}_j\mathbf{E}_j\mathbf{L}_j^{-1}\mathbf{Y}_j. \tag{D1}$$

Let define $\mathbf{C}_j$ such that

$$\mathbf{C}_j = \mathbf{L}_j^{-1}\mathbf{Y}_j \tag{D2}$$

and

$$\mathbf{Y}_{j+1} = \mathbf{L}_j\mathbf{E}_j\mathbf{C}_j. \tag{D3}$$

Redefine $\mathbf{Y}$ to $\mathbf{Y}'$ so that

$$\mathbf{Y}'_{j+1} = \mathbf{L}_j\mathbf{E}_j\mathbf{C}'_j, \tag{D4}$$

where $\mathbf{C}'_j$ is defined such that

$$\mathbf{C}'_j = \mathbf{C}_j\mathbf{Q}_\mathbf{u} = \begin{pmatrix} C_{11} & C_{12} \\ C_{21} & C_{22} \\ C_{31} & C_{32} \\ C_{41} & C_{42} \end{pmatrix} \begin{pmatrix} Q_{u11} & Q_{u12} \\ Q_{u21} & Q_{u22} \end{pmatrix} = \begin{pmatrix} 1 & 0 \\ 0 & 1 \\ C'_{31} & C'_{32} \\ C'_{41} & C'_{42} \end{pmatrix}. \tag{D5}$$

This equation leads to

$$Q_{u11} = \frac{C_{22}}{C_{11}C_{22} - C_{12}C_{21}}, \tag{D6}$$

$$Q_{u12} = \frac{-C_{12}}{C_{11}C_{22} - C_{12}C_{21}}, \tag{D7}$$

$$Q_{u21} = \frac{-C_{21}}{C_{11}C_{22} - C_{12}C_{21}}, \tag{D8}$$

$$Q_{u22} = \frac{C_{11}}{C_{11}C_{22} - C_{12}C_{21}}, \tag{D9}$$

$\mathbf{C}'_j$ contains in each column different wave types together with the corresponding reflections.

D2 Propagation from the half-space to the source

For the wave propagation from the half-space to the source, the matrix of basis vectors can be written as

$$\mathbf{Y}_j = \mathbf{L}_j\mathbf{E}_j^{-1}\mathbf{L}_j^{-1}\mathbf{Y}_{j+1}. \tag{D10}$$

In this case, $\mathbf{C}_j$ is defined such that

$$\mathbf{C}_j = \mathbf{L}_j^{-1}\mathbf{Y}_j. \tag{D11}$$

This leads to

$$\mathbf{Y}_j = \mathbf{L}_j\mathbf{C}_j. \tag{D12}$$

For the layer $j + 1$, we have

$$\mathbf{Y}_{j+1} = \mathbf{L}_{j+1}\mathbf{C}_{j+1}. \tag{D13}$$

We then obtain

$$\mathbf{Y}_j = \mathbf{L}_j\mathbf{E}_j^{-1}\mathbf{L}_j^{-1}\mathbf{L}_{j+1}^{-1}\mathbf{C}_{j+1}. \tag{D14}$$

Reset $\mathbf{C}_j$

$$\mathbf{C}_j = \mathbf{L}_j^{-1}\mathbf{L}_{j+1}\mathbf{C}_{j+1}, \tag{D15}$$

so that

$$\mathbf{Y}_j = \mathbf{L}_j \mathbf{E}_j^{-1} \mathbf{C}_j. \tag{D16}$$

Redefine $\mathbf{Y}'$ so that

$$\mathbf{Y}'_j = \mathbf{L}_j \mathbf{E}_j^{-1} \mathbf{C}'_j, \tag{D17}$$

where $\mathbf{C}'_j$ is defined such that

$$\mathbf{C}'_j = \mathbf{C}_j \mathbf{Q}_\mathbf{b} = \begin{pmatrix} C_{11} & C_{12} \\ C_{21} & C_{22} \\ C_{31} & C_{32} \\ C_{41} & C_{42} \end{pmatrix} \begin{pmatrix} Q_{b11} & Q_{b12} \\ Q_{b21} & Q_{b22} \end{pmatrix} = \begin{pmatrix} C'_{11} & C'_{12} \\ C'_{21} & C'_{22} \\ 1 & 0 \\ 0 & 1 \end{pmatrix}. \tag{D18}$$

This equation leads to

$$Q_{b11} = \frac{C_{42}}{C_{31}C_{42} - C_{32}C_{41}}, \tag{D19}$$

$$Q_{b12} = \frac{-C_{32}}{C_{31}C_{42} - C_{32}C_{41}}, \tag{D20}$$

$$Q_{b21} = \frac{-C_{41}}{C_{31}C_{42} - C_{32}C_{41}}, \tag{D21}$$

$$Q_{b22} = \frac{C_{31}}{C_{31}C_{42} - C_{32}C_{41}}. \tag{D22}$$

In this representation, $\mathbf{C}'_j$ contains in each column different wave types separately together with their corresponding reflections.

APPENDIX E: PSEUDO 4×4 PROPAGATOR MATRIX FOR A WATER LAYER ON TOP OF A LAYERED ELASTIC MEDIUM

In the presence of a water layer, characterized by a shear stress $\mu = 0$, only P waves contribute to the Green's function estimation.

Starting from the wave equation for the *P–SV* case, it can be demonstrated that

$$r_1 = \frac{k}{\rho\omega^2} r_4 \tag{E1}$$

and

$$\begin{aligned} \frac{\partial r_4}{\partial z} &= -\rho\omega^2 r_2 \\ \frac{\partial r_2}{\partial z} &= \frac{1}{\rho\omega^2}\left(-k^2 + \frac{\omega^2}{\alpha^2}\right) r_4 \end{aligned} \tag{E2}$$

$$\frac{\mathrm{d}}{\mathrm{d}z}\begin{pmatrix} r_2 \\ r_4 \end{pmatrix} = \begin{pmatrix} 0 & \frac{1}{\rho\omega^2}\left(-k^2 + \frac{\omega^2}{\alpha^2}\right) \\ -\omega^2\rho & 0 \end{pmatrix}\begin{pmatrix} r_2 \\ r_4 \end{pmatrix}. \tag{E3}$$

This equation is of the form

$$\frac{d\mathbf{r}}{dz} = \mathbf{A}\mathbf{r}, \tag{E4}$$

where

$$\mathbf{r} = \begin{pmatrix} r_2 \\ r_4 \end{pmatrix} \tag{E5}$$

and

$$\mathbf{A} = \begin{pmatrix} 0 & \frac{1}{\rho\omega^2}\left(-k^2 + \frac{\omega^2}{\alpha^2}\right) \\ -\omega^2\rho & 0 \end{pmatrix}. \tag{E6}$$

The solution to eq. (E4) at two points z_1 (at the water surface) and z_2 (at the ocean floor) is (Gantmacher 1959; Gilbert & Backus 1966; Aki & Richards 2002)

$$\begin{pmatrix} r_2 \\ r_4 \end{pmatrix}_{z_2} = \mathbf{P} \begin{pmatrix} r_2 \\ r_4 \end{pmatrix}_{z_1}, \tag{E7}$$

where

$$\mathbf{P} = \begin{pmatrix} \cosh[\gamma(z_2 - z_1)] & -\dfrac{\gamma}{\rho\omega^2} \sinh[\gamma(z_2 - z_1)] \\ -\dfrac{\rho\omega^2}{\gamma} \sinh[\gamma(z_2 - z_1)] & \cosh[\gamma(z_2 - z_1)] \end{pmatrix}. \tag{E8}$$

To obtain the pseudo 4×4 matrix, we rewrite eq. (E7) as follows (see also Herrmann 2008):

$$\begin{pmatrix} r_1|_{z_2} \\ r_2|_{z_2} \\ r_3|_{z_2} \\ r_4|_{z_2} \end{pmatrix} = \begin{pmatrix} 1 & 0 & 0 & 0 \\ 0 & \cosh[\gamma(z_2 - z_1)] & 0 & -\dfrac{\gamma}{\rho\omega^2} \sinh[\gamma(z_2 - z_1)] \\ 0 & 0 & 1 & 0 \\ 0 & -\dfrac{\rho\omega^2}{\gamma} \sinh[\gamma(z_2 - z_1)] & 0 & \cosh[\gamma(z_2 - z_1)] \end{pmatrix} \begin{pmatrix} r_1|_{z_2} \\ r_2|_{z_1} \\ r_3|_{z_2} \\ r_4|_{z_1} \end{pmatrix}. \tag{E9}$$

The pseudo-propagator matrix in terms of eigenvector (**L**) and eingenvalues (**E**) matrices can be given by

$$\begin{aligned} \mathbf{P}_{\text{pseudo}} &= \begin{pmatrix} 1 & 0 & 0 & 0 \\ 0 & \cosh[\gamma(z_2 - z_1)] & 0 & -\dfrac{\gamma}{\rho\omega} \sinh[\gamma(z_2 - z_1)] \\ 0 & 0 & 1 & 0 \\ 0 & -\dfrac{\rho\omega^2}{\gamma} \sinh[\gamma(z_2 - z_1)] & 0 & \cosh[\gamma(z_2 - z_1)] \end{pmatrix} \\ &= \mathbf{L}\mathbf{E}\mathbf{L}^{-1} \\ &= \begin{pmatrix} 1 & 0 & 0 & 0 \\ 0 & -\dfrac{\gamma}{\rho\omega^2} & 0 & \dfrac{\gamma}{\rho\omega^2} \\ 0 & 0 & 1 & 0 \\ 0 & 1 & 0 & 1 \end{pmatrix} \\ &\quad \begin{pmatrix} 1 & 0 & 0 & 0 \\ 0 & \exp[\gamma(z_2 - z_1)] & 0 & 0 \\ 0 & 0 & 1 & 0 \\ 0 & 0 & 0 & \exp[-\gamma(z_2 - z_1)] \end{pmatrix} \\ &\quad \begin{pmatrix} 1 & 0 & 0 & 0 \\ 0 & -\dfrac{\rho\omega^2}{2\gamma} & 0 & \dfrac{1}{2} \\ 0 & 0 & 1 & 0 \\ 0 & \dfrac{\rho\omega^2}{2\gamma} & 0 & \dfrac{1}{2} \end{pmatrix}, \end{aligned} \tag{E10}$$

where $\gamma = \sqrt{k^2 - \omega^2 / V_{\mathbf{P}}^2}$.

From this point on, the algebra is again similar to the derivations presented earlier. The effect of the presence of the water layer on the estimated *H*/*V* spectral ratio curves is discussed in the text.